LAWRENCE LIVERMORE NATIONAL LABORATORY

LLNL-JRNL-560513

LLNL-G3Dv3: global P-wave tomography model for improved regional and teleseismic travel time prediction

N. A. Simmons, S. C. Myers, G. Johannesson, E. Matzel

June 8, 2012

Journal of Geophysical Research

Disclaimer

This document was prepared as an account of work sponsored by an agency of the United States government. Neither the United States government nor Lawrence Livermore National Security, LLC, nor any of their employees makes any warranty, expressed or implied, or assumes any legal liability or responsibility for the accuracy, completeness, or usefulness of any information, apparatus, product, or process disclosed, or represents that its use would not infringe privately owned rights. Reference herein to any specific commercial product, process, or service by trade name, trademark, manufacturer, or otherwise does not necessarily constitute or imply its endorsement, recommendation, or favoring by the United States government or Lawrence Livermore National Security, LLC. The views and opinions of authors expressed herein do not necessarily state or reflect those of the United States government or Lawrence Livermore National Security, LLC, and shall not be used for advertising or product endorsement purposes.

LLNL-G3Dv3: global P-wave tomography model for improved regional and teleseismic travel time prediction

N.A. Simmons[1], S.C. Myers[1], G. Johannesson[2] & E. Matzel[1]

[1]Atmospheric, Earth and Energy Division, Lawrence Livermore National Laboratory
[2]Systems and Decision Sciences, Lawrence Livermore National Laboratory

Corresponding author:

Nathan A. Simmons
L-046
Lawrence Livermore National Laboratory
Livermore, CA 94550
(925) 422-2473
Simmons27@llnl.gov

For submission to *Journal of Geophysical Research – Solid Earth*

Prepared by LLNL under Contract DE-AC52-07NA27344

Abstract

We develop a global-scale P-wave velocity model (LLNL-G3Dv3) designed to accurately predict seismic travel times at regional and teleseismic distances simultaneously. The model provides a new image of Earth's deep interior, but the underlying practical purpose of the model is to provide enhanced seismic event location capabilities. Previous versions of LLNL-G3D provide substantial improvements in event location accuracy due to a more explicit Earth representation from the surface to the core and 3-D ray tracing. The latest model is based on ~2.8 million *P* and *Pn* arrivals that are re-processed using our global multi-event locator known as Bayesloc. We construct LLNL-G3Dv3 within a spherical tessellation based framework, allowing for explicit representation of undulating and discontinuous layers including the crust and transition zone layers. Using a multi-scale inversion technique, regional trends as well as fine details are captured where the data allow. LLNL-G3Dv3 exhibits large-scale structures including cratons and superplumes as well numerous complex details in the upper mantle including within the transition zone. Particularly, the model reveals new details of a vast network of subducted slabs trapped within the transition beneath much of Eurasia, including beneath the Tibetan Plateau. We demonstrate the impact of Bayesloc multiple-event location on the resulting tomographic images through comparison with images produced without the benefit of multiple-event constraints (single-event locations). We find that the multiple-event locations allow for better reconciliation of the large set of direct P phases recorded at 0-97° distance and yield a smoother and more continuous tomographic model than the single-event locations. Travel times predicted from a 3-D model are also found to be strongly influenced by the initial locations of the input data, even when an iterative inversion/relocation technique is employed.

1. Introduction

Numerous global P-wave tomography images of the mantle have been produced primarily for the purpose of understanding the evolutionary processes that occur deep within the Earth [e.g. *Obayashi et al*., 1997; *Su and Dziewonski*, 1997; *van der Hilst et al*., 1997; *Bijwaard et al*., 1998; *Kennett et al.* 1998; *Boschi and Dziewonski*, 1999; *Masters et al*. 2000; *Zhao* 2001; *Fukao et al*. 2003; *Houser et al*., 2008; *Li et al*., 2008; *Simmons et al*. 2010]. Imaging the Earth in 3-D is indeed an important endeavor that is necessary to further our understanding of Earth processes, and P-wave tomography is a major part of that endeavor.

Three-dimensional images of the Earth's crust and mantle also play a role in practical applications including seismic event monitoring. The ability of global-scale 3-D tomography models to predict seismic travel times for future events anywhere on the globe makes them particularly useful for seismic event location prediction. One major difficulty is that models designed to capture large-scale mantle structure are not always capable of accurately predicting regional travel times due to the under-modeled complexities that exist in the crust and upper mantle. Large events may be located fairly well with teleseismic recordings in many instances, however small events require accurate prediction of seismic travel times at regional distances (up to ~15°) as well as intermediate distances (~15-23°) which includes upper mantle triplications. The optimal model should predict seismic arrivals at all distances simultaneously to assure consistency. Therefore development of one model with details in the crust and upper mantle as well as long-wavelength heterogeneity is required.

We address this issue by first establishing a more complex Earth model representation (relative to a purely spherical representation) that explicitly includes the crust (rather than using crustal corrections) and aspherical surfaces including undulating discontinuities from the surface to the core. This complex model design is built within a hierarchical tessellation framework, and facilitates the calculation of 3-D ray paths that honor the variable discontinuity depths. Using 3-D ray paths as the basis for travel time prediction and model sensitivity, we develop a new global P-wave tomography model called LLNL-G3Dv3.

The model is derived from a collection of ~2.8 million direct P-wave arrivals recorded at distances from 0 to about 97°. The seismic events are located with the multi-event location algorithm called Bayesloc [*Myers et al.* 2007, 2009, 2011]. Bayesloc is a formulation of the joint probability distribution across multiple-event location parameters, including hypocenters, travel time corrections, pick precision, and phase labels. Modeling the whole multiple-event system results in accurate locations and an internally consistent data set that is ideal for joint regional and teleseismic tomography [*Myers et al.* 2011; *Simmons et al.* 2011]. We adapt the Bayesloc algorithm in this study to accommodate regional structural trends by incorporating variable regional travel time curve adjustments for improved location estimates. We evaluate the importance of accurate initial event locations of the input data prior to tomographic inversion through comparison with an alternative approach involving iterative tomographic inversion and relocation. Thus, this study has two parallel components: development of a new tomographic model to advance our understanding of the Earth, and evaluating the impact of prior event location accuracy on the prediction of travel times computed with the outcome tomographic model.

2. Data

Travel time data were gathered from the Lawrence Livermore National Laboratory (LLNL) database [see *Ruppert et al*., 2005], which is a massive compilation of data from a variety of sources. Those include the EHB bulletin [Engdahl et al., 1998] provided by the International Seismological Centre (ISC, http://www.isc.ac.uk), the National Earthquake Information Center (NEIC, http://earthquake.usgs.gov/regional/neic) bulletin, and a variety of regional bulletins. Additional data are derived from seismic deployments for Peaceful Nuclear Explosions (PNE's), large refraction surveys, the USARRAY Transportable Array (TA) and temporary PASSCAL deployments (http://www.iris.edu) around the world. A large number of the travel time measurements were made by staff at LLNL. Currently, the full travel time data consists of ~13.4 million measurements from ~118,000 seismic events.

Given the redundancy of very large tomography data sets, many studies choose to combine the information by forming summary rays through simple averaging or a more sophisticated process that is outlined in *Myers et al.* [2011] and repeated here for completeness. Instead of forming summary rays, we chose to select specific events to be simultaneously relocated with Bayesloc. Therefore, we designed an event selection strategy to find seismic events with the highest probability to be accurately located using the Bayesloc procedures and events that provide the greatest number of P and Pn data for tomography. The selected events include all available Ground Truth level 5 (GT5) or better based on the *Bondár et al.* [2004] criteria. In addition, we selected events with the most:

1) teleseismic *P* travel time measurements,

2) even azimuthal coverage of the teleseismic networks as measured using the criteria of *Bondár and Mclaughlin* [2009],
3) regional *Pn* travel time measurements, and
4) local *Pg* measurements provided that *Pn* or *P* measurements exist for the event.

Sampling was achieved by rank-ordering events based on the four criteria. The first event in the list was selected and other events within 1° were removed from consideration for that criterion. Event sampling with the above selection criteria was repeated for events in 6 depth bins: 0-35 km, 35-75 km, 75-150 km, 150-300 km, 300-450 km and 450-700 km depth range.

Through this selection process, we reduced the number of considered events to 13,069 of the global seismic events with the most measurements and the best network geometry. The selected events provided ~3.4 million travel time measurements for a suite of teleseismic, regional, and depth phases (Table 1) recorded at 7,370 seismic stations worldwide. We find that the event selection provides little or no loss in global data coverage.

3. Methods

3.1 Bayesloc Multi-event Relocation

Bayesloc is a formulation of the multiple-event location system that includes travel-time corrections, arrival-time measurement (pick) precision, and stochastic phase labels. The hierarchical Bayesian formulation allows for prior constraints on any aspect of the multiple-event system, and a Markov-chain Monte Carlo method is used to draw samples from the joint distribution of multiple-event location parameters. A full description of the Bayesloc methodology can be found in *Myers et al.* [2007, 2009] and application to a global data set is described in *Myers et al.* [2011].

The Bayesloc travel-time correction formulation includes a correction to the travel time curve for each phase, which accounts for regional travel-time error trends. To the travel time curve corrections, Bayesloc adds station and event terms with a zero-mean prior constraint to account for small, path-dependent errors. *Myers et al*. [2011] relocated a set of global events, but limited regional-distance travel time data to the Middle East. Therefore, one adjustment for each regional-phase travel time curve was sufficient. In this study we include regional-phase data from all parts of the globe, which necessitates spatially variable corrections to regional-phase travel time curves. Varying regional travel time curve corrections are achieved by forming a cluster of neighboring events around each event and simultaneously relocating the cluster. In addition to allowing for region-specific travel-time curve corrections, simultaneous relocation of event clusters maintains the ability to propagate prior constraints from GT0-GT5 through the data set and provides robust estimates of pick precision and phase labels.

In this application we first relocated all events using Bayesloc, but without travel time corrections. This step takes advantage of Bayesloc's stochastic phase labels and pick precision based on phase and station components. Stochastic phase labels mitigate gross data errors and modeling pick precision has the affect of up-weighting phases and stations for which data are consistent throughout the whole data set. In the second step, event clusters are formed for each event. To ensure that corrections to regional travel time curves are applicable to all events in a cluster, only events within 500 km are considered in the formation of an event cluster. Robustness tests for the constraint of Bayesloc parameters were used to set the minimum number of events for a cluster at 20. The number of events in a cluster is limited to 40, because there is little improvement in the constraint of Bayesloc parameters when additional events are added. The variable geographic extent of the event clusters is shown for 4 examples in Figure 1. Event clusters are typically 100 km to 200 km across in seismically active continental regions. Cluster size expands for ocean ridge events that gather events along a linear trend, and cluster size expands to the full 500 km radius in aseismic regions.

Bayesian (probabilistic) constraints on location parameters were enforced for events with well-constrained epicenters, depth, and/or origin times. Many of the events are explosions with known hypocenters. However, origin times are unknown for many explosions, and our prior constraints reflect the origin time uncertainty. Geographic coverage of events with location priors is greatly improved by including events that meet the GT5 criteria of *Bondár et al.* [2004]. *Bondár et al.* [2004] find that an epicenter can be conservatively determined to within 5 km (at 95% confidence) using the ak135 model [*Kennett et al*., 1995] for travel time predictions and first-arriving P-waves at a network with: at least 10 stations within 250 km of the event; a network azimuthal gap of less than 110°; a secondary network azimuthal gap of less than 160°; and at least one station within 30 km. Most bulletin events use all available data, including secondary phases and data at stations beyond 250 km. We identify events with sufficient data to meet the GT criteria, and relocate them events using only P-wave arrivals within 250 km. An epicenter prior is then enforced in the Bayesloc analysis for event locations passing all GT5 after relocation.

The global data set consists of 13,069 events and 3,406,407 picks. Table 1 lists the number of picks by phase, showing that locations are predominantly constrained by teleseismic P-wave arrivals times. Not only do P-waves account for over 78% of the data set, but P-wave measurement precision (and therefore data weight) is on average 1 ½ times greater than the next most precisely measured phase (Pn), as reported by *Myers et al*. [2011]. Surface reflected phases (pP and sP) are also included in the data set to constrain event depth. However, we note that measurement precision for pP and sP are 5 to 10 times lower than for P [*Myers et al*., 2011], so constraining hypocenter depth remains problematic for many events.

Travel-time priors follow the approach taken in *Myers et al*. [2011]. Corrections to travel time curves include an adjustment to the slope and intercept. Because we use the ak135 model for travel times, the teleseismic-phase travel time curves (P, pP, sP, PcP) are already optimized by *Kennett et al*. [1995], which allows us to place tight constraints on corrections for those travel time curves. Conversely, we place loose constraints on the slope and intercept of regional-phase travel time curves (Pn, Sn, Pg, Lg), allowing Bayesloc to force regional curves to be consistent with teleseismic travel times.

Bayesloc multiple-event processing results in median epicenter shifts of 6.8 km, depth shifts of 5.5 km, and origin time shifts of -0.67 seconds compared to single-event locations (Figure 2). Figure 2 shows that epicenter shifts are not random, but rather regionally dependent. The largest shifts are observed at subduction zones, where events tend to move trenchward, which is consist with the observations and reasoning of *Creager and Boyed* [1992]. Epicenter shifts for many events in the Former Soviet Union are small because events are predominantly explosions with known locations that are constrained by priors.

After Bayesloc processing we remove events if the 90% epicenter probability region for that event exceeds 1000 km^2 in area. Events are also removed if the depth uncertainty exceeds 18 km or if the origin time uncertainty exceeds 1 second. Individual travel time picks are removed if the phase label is not determined with probability greater than 0.95 or if arrival-time uncertainty is greater than 1 second. Based on these criteria, the number of events is reduced to 12,571 (3.8% reduction) and the number of P and Pn picks is reduced from 2,948,378 to 2,820,062 (4.3% reduction). Relocation using Bayesloc and removal of a relatively modest percentage of untrusted data results in a reduction in travel time residuals (w.r.t. ak135) from 1.59 seconds to 1.26 seconds, which equates to a 37% reduction in variance (Figure 3).

As a test of location accuracy, we relocated all events without the benefit of any event-location priors. To mitigate the influence of poor data, we utilized the Bayesloc data set with poorly constrained events and low-precision or erroneous picks removed. We then measured the difference between estimated epicenters and epicenters with known accuracy of 1 km or better. The mean and median location difference between Bayesloc and known epicenters is found to be 4.06 km and 3.2 km, respectively. By comparison, the mean and median location error is found to be 6.22 km and 5.36 km, respectively, when events are located one at a time and using the same arrival-time data set.

3.2 Model Architecture

The LLNL-G3Dv3 model is parameterized with nodes defined by triangular tessellations of spherical surface (Figure 4). Spherical tessellation grids have been employed in numerous global geophysical studies primarily for generating evenly spaced points and avoiding polar distortions created by latitude-longitude grids [e.g. *Baumgardner and Frederickson*, 1985; *Constable et al*., 1993; *Wang and Dahlen*, 1995; *Chiao and Kuo*, 2001; *Ishii and Dziewonski*, 2002; *Antolik et al.* 2003; *Sambridge and Faletič*, 2003; *Peter et al*., 2007; *Ballard et al*., 2009; *Gung et al*., 2009; *Stockmann et al.*, 2009; *Myers et al.* 2010; *Simmons et al.* 2011]. Spherical tessellation grids are designed through a process known as dyadic refinement [see *Baumgardner and Frederickson*, 1985] and are conveniently extensible to any resolution level.

Recently, studies by *Ballard et al*. [2009] and *Simmons et al*. [2011] demonstrate the ability to construct complex Earth models within a tessellation-based framework while preserving efficient means of communication with the models. Specifically, designing a spherical tessellation mesh is a recursive process and each subdivision step produces a new level in the grid hierarchy. The grid hierarchy may be exploited through a hierarchical version of the triangle search method [*Lawson* 1984] to determine properties of surrounding points in a lateral sense. To construct model layers, nodes are placed along geocentric vectors defined from the center of spherical tessellation grid through the intersections of the triangles (vertices). Nodes are simply placed at variable radii along the geocentric vectors to explicitly characterize undulating surfaces. Discontinuities are defined by double nodes placed at the exact same location (with different properties such as velocity), and multiple layers are allowed to intersect (i.e. pinch out). Thus, the model architecture is a more explicit representation than spherical descriptions of the Earth which are often employed in global-scale tomography studies. In particular, we can directly incorporate the complexities of the crust rather than computing *crustal corrections* which are common in global-scale tomography studies. See *Simmons et al.* [2011] for more details regarding our specific model design and communication techniques.

Similar to the *Simmons et al.* [2011] study, we chose to develop a fully 3-D starting model by leveraging several previous studies. The motivation to begin with a 3-D model is multi-fold. Based on numerous past studies, we have a basic understanding of the 1st order Earth structure including: i) continental crust tends to be thick while oceanic crust is thin, ii) continental platform/cratonic regions have fast upper mantles while tectonically active regions are relatively slow, iii) spreading centers such as mid-ocean ridges and rifts tend to be slow, iv) mantle wedges along convergent margins are slow while subducted slabs tend to be fast, v) depths of the upper mantle transition zone discontinuities vary, and vi) massive low-velocity superplumes and ancient fast slab remnants exist in the lower mantle. P-wave travel times are sensitive to all of the structural elements, even though tomography using a P and Pn data set cannot fully resolve many of these features including mid-ocean ridges and discontinuity depths. Therefore, to create a model with predictive abilities, we believe that it is important to begin with *a priori* 3-D structures that more closely resemble the actual Earth than a 1-D model.

For the starting model crustal structure, we use a modified version of the 'Unified' crust model which is joint national laboratory effort [*Pasyanos et al*., 2004; *Steck et al*. 2004]. The model is based on a compilation of geophysical information regarding crustal structure throughout Eurasia and North Africa (0-90°N latitudes and 20°W to 150°E), modified during the development of the Regional Seismic Travel Time (RSTT) model [*Myers et al*., 2010]. The crustal model is made up of 7 discontinuous layers including a water/ice layer, 3 sediment layers, and 3 crystalline crust layers. Beyond the Eurasia/North Africa region, we employ the Crust 2.0 model [*Bassin et al*., 2000]. We further leverage the RSTT model (consisting of mantle velocity at the Moho and mantle velocity gradient with depth) to design a shallow upper mantle P-wave velocity model in the Eurasia/North Africa region defined above. In particular, we use the RSTT P-wave velocities at the Moho and extrapolate velocities to 115 km depth using the RSTT velocity gradient term [see *Myers et al*., 2010].

For the remaining mantle velocities (everywhere except the shallow upper mantle beneath Eurasia and North Africa), we adopt the P-wave velocity structure of the GyPSuM model [*Simmons et al*. 2010]. GyPSuM is a mantle-scale model of seismic wave speeds (P and

S) and density constructed through a joint inversion of seismic, geodynamic, and mineral physics constraints. The model is the culmination of past investigations to simultaneously reconcile seismic and geodynamic observations [see *Simmons et al*. 2006, 2007, and 2009]. The seismic constraints consist of teleseismic P-wave travel times (P phase only) and S-wave travel times (S, sS, ScS, SKS, SKKS and a variety of surface reflected multiples). The geodynamic constraints include global free-air gravity, tectonic plate motions, dynamic topography of the surface, and the excess ellipticity of core mantle boundary. The GyPSuM model provides estimates of heterogeneity (where certain constraints are lacking) through coupling multiple types of data (seismic, geodynamic, and mineral physics). Most importantly for this study, GyPSuM provides reasonable estimates of P-wave velocity structure in regions that are under-sampled by P-wave phases themselves and/or simply not resolvable with P-wave information alone.

Owing to the substantial variation in depth of the upper mantle transition zone discontinuities [e.g. *Flanagan and Shearer*, 1998; *Gurrola and Minster*, 1998; *Lawrence and Shearer*, 2008; *Deuss*, 2009], we perturbed the depths of the ‘410’ and ‘660’ discontinuities according to the global high-resolution SS precursor study of *Lawrence and Shearer* [2008]. Our choice to perturb these boundaries stems from the reality that our data cannot independently resolve the depth of the discontinuities and velocities simultaneously due to severe trade-offs. The final external constraint incorporated into our model is the oblateness of the Earth. This is achieved by projecting layers in the radial direction in order to conform to the WGS84 ellipsoid and the expected hydrostatic shape of the mantle and core [*Nakiboglu*, 1982; *Alessandrini*, 1989]. This final step eliminates the requirement for ellipticity corrections since Earth’s asphericity is directly built-in.

The LLNL-G3Dv3 model (starting model and the tomographic solution) consists of a crust and upper mantle that are represented by 31 layers, defined at nodes with ~1° lateral spacing (mesh created by 6 recursive triangular sub-divisions of an icosahedron, referred to as the 'level 7' tessellation grid). The lower mantle is represented by 26 layers, defined at the tessellation grid level 6 (~2° node spacing). All together, the model consists of 57 layers from the surface to the core and about 1.6 million model nodes. See Figure 4 for a summary of the model architecture.

3.3 Three-dimensional Ray Tracing

The effort to generate complex global-scale tomography models is motivated by the fact that accurate model-based travel time prediction necessitates 3-D ray tracing given significant ray path discrepancies between 1-D and 3-D ray paths [*Zhao and Lei*, 2004]. Deviations in the ray paths from the 1-D assumption are particularly large where high degrees of velocity variability exist, such as in the shallow upper mantle where regional rays travel. Thus, we adapted a 3-D ray tracing approach based on the *Zhao et al*. [1992] methodology. The ray tracing algorithm is an iterative procedure that adjusts an initial path to satisfy Snell's law across discontinuities and bends paths based on the pseudobending technique within the continuous media [*Um and Thurber*, 1987]. The method was recently modified by *Simmons et al.* [2011] to find absolute minimum travel time paths, which often differ greatly from an initial path based on a 1-D Earth model. As an example, we considered an event 20 km below the Japan region (Figure 5). For simplicity, we placed 6 *hypothetical stations* along a great circle path into northeastern Asia and computed ray paths for the ak135 model [*Kennett et al*., 1995] and the 3-D model developed in this study (LLNL-G3Dv3) for comparison. In this example, the minimum time ray paths dive significantly deeper than the 1-D model would suggest due to the high velocities associated with the subducting slab beneath Japan, compounded by the low-velocity wedge in the upper mantle that the minimum time paths tend to avoid. At distances of ~18-24°, the minimum-time ray paths are also focused into the high-velocity slab structures observed within the transition zone layer.

Clearly the minimum-time ray path is strongly dependent on the underlying velocity model, which is particularly problematic at regional distances if ray paths are to be based on global average 1-D Earth models such as PREM [*Dzeiwonski and Anderson*, 1981] or ak135 (used in our example above). We demonstrate the potential differences between 1-D and 3-D ray paths at regional distances in Figure 5, but it has also been shown by *Zhao and Lei* [2004] that even teleseismic paths and travel time predictions are subject to 3-D effects.

Using a 1-D model is also troublesome in the context of defining model sensitivity for tomographic inversion since velocity anomalies would clearly be projected to the wrong portions of the model. With paths based on a 1-D model, it may be possible to predict a given set of travel time data just as well as with 3-D ray paths; however, the image will be incorrect and the ability to predict travel times for future arrivals is therefore diminished. In addition to 1-D/3-D ray path discrepancies, multi-pathing is a significant problem [e.g. *Simmons et al*., 2011]. Therefore, we define model sensitivity using multiple ray paths that theoretically arrive at a station within a short time window (we use 0.2 seconds). See *Simmons et al*. [2011] for a more thorough description of our ray tracing procedures including the calculation of multi-paths, and the development of sensitivity kernels for tomographic inversion.

3.4 Imaging Process

Inversions are performed using the multi-scale inversion technique called *Progressive Multi-level Tessellation Inversion* (PMTI) developed in *Simmons et al.* [2011]. The PMTI procedure is a valuable technique for inverting mixed-determined systems and is thus ideal for seismic tomography. The procedure leverages the hierarchical nature of the tessellation-based model design and images long-wavelength features in regions with sparse data, while also imaging fine details where data are sufficient. PMTI is akin to multigrid [e.g. *Zhou*, 1996] and wavelet-based approaches [e.g. *Chiao and Kuo*, 2001] in which higher resolution solutions are cast as perturbations to a lower resolution model. The PMTI process involves: i) first determining the longest-wavelength structure, ii) removing the effects of that structure from the data, iii) then progressively solving for shorter wavelength anomalies to further reconcile the data. The process may be compared to a spherical harmonic decomposition approach whereby low-degree terms are determined followed by higher degree harmonics. However, the PMTI process may be performed with local parameter bases that reduce artifacts in regions with poor data coverage relative to global basis definition [*Boschi and Dziewonski*, 1999]. As demonstrated in *Simmons et al.* [2011], additional benefits of the PMTI approach include: i) intrinsic regularization allowing for reasonable models with only a global damping parameter, ii) avoiding the design of irregular meshes and/or regional mesh refinement schemes based on *ad hoc* criteria, and iii) no need to calculate wavelet transforms or invert structure on multiple grids simultaneously.

To perform a single round of PMTI, we compute sensitivity kernel matrices for 7 lateral resolution levels (tessellation levels 1-7) and subsequently solve for slowness perturbations at each level in sequence. In contrast to the *Simmons et al*. [2011] study, we also consider variable depth resolutions. This is achieved by effectively combining layers contained in the full model and solving for slowness perturbations for all layers in the group simultaneously (i.e. adjusting the stack of layers with a single slowness perturbation). For example, at the lowest lateral resolution level (~63° spacing) we combine model layers into 3 total inversion layers: i) the crust, ii) the upper mantle, and iii) the lower mantle (see Figure 6). At the highest lateral resolution level (~1° spacing), all layers are allowed to adjust independently with the exception of crustal layers. We combine all crustal layers and adjust the entire stack simultaneously throughout the process since our constraints on the details of the crust are lacking.

In the final stage of the PMTI process (level 7), there are 45 layers and >1 million free parameters in the inversion. As resolution increases, the number of model parameters grows rapidly; and increasing the resolution in many regions (such as the upper mantle beneath ocean basins) becomes excessive. This makes irregular parameterizations attractive for global-scale modeling, whether the parameters are statically defined prior to inversion [e.g. *Bijwaard and Spakman*, 1998; *Li et al*. 2008] or refined within an inversion process [e.g. *Sambridge and Faletič*, 2003]. However, using the PMTI approach, irregular grid design is unnecessary for global and regional-scale tomographic imaging. With modern computational platforms, development of a global upper mantle model with 25 km resolution is manageable. *Simmons et al*. [2011] demonstrated that maintaining a regular grid in the lateral extent (rather than regional mesh refinement) produces little or no computational hindrance when storing the model or performing the inversion. This assertion is re-iterated in the current study with a much larger system of equations and larger set of free parameters relative to the previous study. As demonstrated in Table 2, the size of the tomographic system grows as resolution increases. However, owing to the increasing sparseness of the tomographic systems of equations with resolution level, the rate of matrix growth is *not* proportional to the rate of added model nodes. Thus, the important quantity is not the number of free parameters, but rather the average number of sensitive nodes per datum. In sparsely sampled regions, a large number of nodes will not be involved in the inversion simply because no data are sensitive to them. It follows that these un-sampled nodes do not contribute to the size of the sensitivity matrix given that sparse matrix algorithms are employed. In our case, the largest system of equation (sensitivity kernel matrix) is 12.5 Gbytes and the total time to complete the PMTI process is less than 0.5 hours with a single modern CPU (Table 2).

PMTI is one important component in the imaging process; however the *overall* imaging process involves multiple steps to account for the interdependence of ray paths and velocity structure which presents a non-linear problem. We execute an iterative process whereby PMTI imaging is performed and 3-D ray paths are re-computed at each step (Figure 7). The global damping weight is initially set at some maximum value and relaxed at each step until the pre-determined minimum damping is achieved. The damping weights were determined by calculating the trade-off between data misfit and model complexity (L-curve analysis, Figure 8).

Although the new models developed at each step are used to define new 3-D ray paths and sensitivity kernels, travel times are calculated along the new 3-D ray paths projected through the starting model. Thus, travel time residuals are always computed with respect to the starting model regardless of the model used to compute the 3-D ray paths. Therefore, all inversions result in slowness perturbations relative to the starting model, rather than an intermediate model used to determine ray paths. This procedure prevents artifacts in the model we refer to as '*ghost anomalies*'.

We illustrate the ghost anomaly concept in Figure 7 with a hypothetical example. In our illustrative example, an earthquake is placed within a subducting slab that is initially un-imaged. The energy arrives at the seismic station early, and our starting model predicts that the minimum time path travels across the shallow mantle (dashed line in Figure 7). If our initial minimum-time ray path is erroneous due to inaccuracies of the starting model, anomalies may be projected to the wrong location in the model. In this scenario, other data have begun to image the fast slab anomaly. It follows that the minimum-time path for the recorded arrival now dives down the slab and avoids the shallow high-velocity anomaly generated in the previous step. If we do not revert to the starting model (thereby removing anomalies determined by the previous inversion), the shallow mantle anomaly will remain as part of the new model, yet no paths travel through the structure (i.e. ghost anomaly). The hypothetical example shown in Figure 7 is indeed an extreme case, but one can imagine that as minimum-time ray paths evolve during the imaging process, small remnant structures and image smearing will occur. Our process of reverting back to the starting model before each inversion consequently results in a final model that is closest to the starting model while considering the non-linear aspect of the problem.

4. The LLNL-G3Dv3 Model

4.1 Resolution Tests

Resolution tests were performed employing the PMTI method and P-wave data coverage discussed in previous sections. Given that our goals are to robustly image long- and short-wavelength features simultaneously, we devised a multi-scale checkerboard pattern for resolution analysis (Figure 9). Similar to the tests performed in *Simmons et al.* [2011], the smallest squares are 5° × 5° and each block is part of a much larger regional anomaly. The pattern was duplicated at each layer in the model with opposite signs, generating a very complex layered synthetic model. The upper mantle proves difficult to resolve with P-wave data alone; however details in the shallowest mantle may be imaged in regions with large amounts of regional travel time data. In particular, this complex model is recoverable from top to bottom beneath large portions of Eurasia and North America.

As noted in past studies with vast amounts of P-wave travel time data [e.g. *Li et al.*, 2008], it is difficult to resolve structures beneath ocean basins, particularly beneath the central Pacific and ocean basins in the southern hemisphere. This reiterates the importance of performing joint inversions of multiple data types and/or employing a reasonable starting model based on previous studies. The lack of resolution in the upper mantle and beneath ocean basins is the primary motivation to employ the GyPSuM model [*Simmons et al*., 2010] as a starting solution in this study.

The synthetic checkerboard model with alternating layers is an unrealistic analogy to Earth structure and is clearly an overly rigorous test. Thus, we also performed resolution tests with checkerboards patterns attributed to individual layers rather than all layers simultaneously (Figure 10). With one layer at a time, we begin to recover structure much better within the upper mantle and beneath ocean basins. Both synthetic tests (shown in Figure 10) provide valuable insight into our ability to resolve P-wave velocity anomalies on global and regional scales simultaneously.

4.2 Cratons, Spreading Centers, and Shallow Convergent Margins

Long-wavelength features in the shallow upper mantle are depicted where P-wave coverage is limited (see resolution tests in Figures 9-10). As noted in *Simmons et al*. [2010], joint inversion of multiple data types that include seismic and geodynamic constraints is a powerful way to estimate heterogeneities where singular types of data may provide only limited constraints. Specifically to this modeling effort, it is extremely difficult to resolve reasonable images of P-wave velocity heterogeneity associated with mid-ocean ridges and entire cratons without inversions including surface-reflected multiples and/or surface waves [e.g. *Masters et al*., 2000; *Zhao* 2009]. Since our starting model is based on the joint seismic-geodynamic model (GyPSuM), many of the shallow regions with considerable data gaps are filled in with reasonable estimates of velocity heterogeneity. Thus large portions of the velocity anomalies attributed to cratonic roots and linear mid-ocean ridge structures are also seen as dominant structures in the LLNL-G3Dv3 model (Figure 11).

Although many of the long-wavelength shallow upper mantle structures are largely seen in the starting model, it is important to note that some of the more dramatic differences between LLNL-G3Dv3 and GyPSuM occur within the shallow upper mantle (Figure 13). Specific notable differences include faster velocities beneath the central Asian upper mantle along the Tethyan margin extending far into the continental interior, lowered velocities along convergent margins, and faster velocities along the linear subducted slab structures below ~100 km depth.

Details in the shallow upper mantle P-wave velocity structure are imaged in several regions; particularly where data are abundant such as beneath the North American continent and large portions of Eurasia. Complex velocity structures are clearly evident along tectonic margins, where active seismicity yields numerous data providing powerful constraints. However, we note that complexities in the shallow upper mantle are also found well within the stable continental interiors of North America and Eurasia, where substantial regional travel time data exist as well. These mostly stable cratonic/platform regions are clearly less complex than tectonically active regions and are generally imaged as long-wavelength features. However, stable continental regions may be more complex than generally recognized, due to a lack of resolution.

4.3 Subducted Slabs in the Transition Zone

Like many previous global P-wave tomography studies, we image tabular subducted slabs in the upper mantle along most of the world's active (or recently active) convergent margins (Figure 11) and ancient slabs in the lower mantle (Figure 12). We also detect large high-velocity structures within the transition zone beneath much of Eurasia, which are likely subducted slabs deflected horizontally near the 660-km discontinuity and trapped within the transition zone. Portions of the slabs beneath Eurasia may eventually penetrate into the lower mantle, but may not "maintain their original configuration", as noted two decades ago for the Western Pacific margin [*Fukao et al*., 1992]. These trapped slab structures beneath the Eurasian continental interior tend to have sharper velocity gradients along the edges and are more expansive in the LLNL-G3Dv3 model than most global P-wave models [e.g. *van der Hilst et al*., 1997; *Bijwaard et al.*, 1998; *Kennett et al.* 1998; *Masters et al*. 2000; *Fukao et al*., 2003; *Li et al*., 2008]. In this regard, one of the more comparable global P-wave models is presented in

Zhao [2001]. We find evidence of horizontally deflected slabs (at least partially) in the transition zone in other parts of the world (Figures 14-17), but the vast network of slabs and slab remnants occupying the transition beneath much of Eurasia is most distinctive.

Along the western Pacific margin, the fast anomalies in the transition zone have long been identified as subducted Pacific lithosphere deflected near the base of the upper mantle. Some examples of the deflected slabs beneath East Asia are seen in Figure 17. We also detect a broad fast anomaly above and within the transition zone beneath western China. The anomaly extends from India to Mongolia and lies directly beneath the Tibetan Plateau (see Figure 11). This broad fast anomaly is possibly a large remnant slab subducted during the convergence of India with Eurasia and thus the closing of the Tethys Oceans. It has proven difficult to identify enough subducted lithosphere in the Tethys region from tomographic images to account for the expected volume of slabs subducted since the Mesozoic Era [*Hafkenscheid et al.*, 2006]. It is apparent that substantial quantities of lithosphere has subducted into the lower mantle deep beneath present-day India, contributing to the estimated volumetric budget of subducted material. However, our model indicates that a large volume of the subducted material is trapped in the transition zone beneath most of western China (Figure 16).

Slab structures in the upper mantle are imaged nicely in various tomographic studies including *Li et al*. [2008] which compares well to our model in this regard (Figures 14-17). The stagnation of slabs either within or near the transition zone is also well documented [see *Fukao et al*., 2001]. However, the exact amplitudes, abruptness, and lateral extent of the velocity anomalies differ across all models. The differing details in the transition zone (LLNL-G3Dv3 versus other P-wave models) stem from a number of modeling differences including re-location processes, datasets, model architectures, and imaging techniques. Most notably, without incorporating P-wave arrivals recorded at regional (up to ~15°) and intermediate distances (~15-23°), details in the upper mantle transition zone P-wave velocities are difficult to resolve. Moreover, one of the primary causes of the differences from numerous models of the transition zone is likely the effects of 3-D ray tracing that tends to focus the minimum time ray paths into the transition zone where fast anomalies reside, as opposed to rays based on 1-D models that are indifferent to regional lateral velocity variations. As clearly demonstrated in the ray tracing example in Figure 5, 3-D ray path effects are most significant at regional and intermediate distances and paths computed from a 1-D model are unsuitable for detailed tomographic imaging of the upper mantle including the transition zone.

4.4 Lithospheric Slabs in the Lower Mantle

Many of the large-scale lower mantle anomalies observed in the LLNL-G3Dv3 model are commonly seen in previous global P-wave tomography studies [e.g. *Obayashi et al*., 1997; *van der Hilst et al*., 1997; *Bijwaard et al*., 1998; *Boschi and Dziewonski*, 1999; *Kárason and van der Hilst*, 2000; *Zhao* 2001; *Fukao et al*. 2003; *Li et al*., 2008] and those derived with P- and S-wave data [e.g. *Su and Dziewonski*, 1997; *Kennett et al.* 1998; *Masters et al*. 2000; *Houser et al*., 2008; *Simmons et al*. 2010]. Specifically, most modern global P-wave tomography models depict tabular fast velocity structures beneath the Americas and Eurasia/India at mid-mantle depths that are commonly attributed to ancient subducted plates [*Grand et al*. 1997; *van der Hilst et al*. 1997]. These linear features are clearly seen in current model from ~700-1600 km depth (Figure 12). Compared to the GyPSuM starting model, the ancient slab remnants appear narrower and more defined in the LLNL-G3Dv3 model owing to the increased number of recordings, higher resolution parameterization, and 3-D ray tracing.

The ancient Farallon plate is sinking beneath the eastern coast of the United States (Figure 14, section 1), and the slab signature abruptly diminishes near 1600 km depth. Without more information, this might imply that the slab does not penetrate beyond mid-mantle depths or is disconnected from the apparent slab remnants near the core-mantle boundary. However, as noted in *Simmons et al.* [2010], fast P-wave anomalies associated with subducted slab remnants may be muted at mid-mantle depths due to the opposing effects of electronic spin transitions. Moreover, the effects of electronic spin transitions might explain why fast S-wave anomalies persist through the middle of the lower mantle, while P-wave anomalies become muted. The actual effects of spin transitions on mantle material is highly uncertain, but these effects may pose an alternative to compositional origins for the muting of P-wave velocities in the ancient slab structures [see *Badro et al*., 2003, 2004; *Hofmeister*, 2006; *Lin et al*., 2007, 2008; *Speziale et al*., 2007; *Stackhouse et al*., 2007; *McCammon et al*., 2008; *Crowhurst et al*., 2009; *Wentzcovitch et al*., 2009].

A remnant of the Farallon plate, the Cocos plate, is subducting beneath Central America and appears to be still connected to the massive Farallon plate today (Figure 15, section 1). The connection of the Cocos to the Farallon is also seen in *Li et al*. [2008], and the continuity of the structure appears even more apparent in the LLNL-G3Dv3 model. The Nazca plate, another remnant of the Farallon plate, can be seen in the lower mantle in the northern half of the South American continent. The subduction of the Nazca plate abruptly changes character south of central Bolivia where it is then deflected into the transition zone (Figure 15).

Analogous to the Farallon system of ancient and modern slabs, numerous subducted features are observed beneath southern Eurasia and India along the Tethyan margin (Figure 16). However, the overall slab configurations are more complicated than those observed beneath the Americas, owing to the more extensive and complex tectonic history in the region. See *Hafkenscheid et al.* [2006] for an excellent integrated analysis of the subduction history along the Tethyan margin.

Aside from the classical Farallon and Tethys anomalies, our model suggests that the central Pacific Ocean may have been another site for ancient subduction. A linear fast structure with similar amplitudes as the Farallon and Tethys anomalies appears near 1200 km depth extending from the Aleutian Island chain to the Tonga/Fiji region in the southern Pacific (Figure 12). The mid-Pacific linear high-velocity feature is also visible in the GyPSuM starting model, but appears more prominent in the LLNL-G3Dv3 model. Although it is not typically seen in other global P-wave models, very faint signatures of the anomaly may be seen in the models presented in *Bijwaard and Spakman* [1998] and *Zhao* [2001]. It is believed that an ancient plate known as the Izanagi plate must have existed [*Woods and Davies*, 1982] and it may have bordered the Farallon and Pacific plates near the center of the Pacific Ocean ca. 100 Ma [*Torsvik et al*., 2010]. Perhaps the Farallon-Izanagi and/or Farallon-Pacific plate boundaries were convergent at some point in the mid-Mesozoic Era and the observed linear high-velocity structure beneath the present-day central Pacific is a relic subducted slab. The feature emerges in one of the least well-constrained regions in the mid-mantle (Figure 10), thus more extensive analysis must be performed to confirm the existence of the feature and provide a concrete interpretation based on plate reconstruction analysis. This is clearly beyond the scope of the current study.

4.5 Deep Mantle Heterogeneity

Similar to many previous global tomography studies, we find that the dominant anomalies in the deep mantle (>1600 km depth) are the low-velocity superplume structures beneath Africa and the Pacific Ocean. The superplume structures are robust features in global tomography models and are likely chemically distinct from the surrounding mantle based on the abruptness of the velocity anomalies and apparent intrinsic high-density associated with them [e.g. *Ritsema et al*. 1998; *Ishii and Tromp*, 1999; *Ni et al*., 2002; *Trampert et al*. 2004; *Tan and Gurnis*, 2005; *Simmons et al*. 2007; *Sun et al*., 2010]. These massive low-velocity anomalies are dynamically significant. In particular, studies suggest that the strong upward flow of the African superplume significantly contributes to shallow mantle flow and is possibly responsible for numerous physiographic features on the African continent [*Nyblade and Robinson*, 1994; *Lithgow-Bertelloni and Silver*, 1998; *Gurnis et al*., 2000; *Behn et al*., 2004; *Forte et al*. 2010]. We note that the important superplume structures are largely unchanged from the GyPSuM starting model from the mid-mantle down. Therefore, we refer the reader to *Simmons et al*. [2007, 2010] for more discussion.

The most notable differences between LLNL-G3Dv3 and GyPSuM occur near the base of the mantle beneath East Asia and the Pacific Ocean which becomes somewhat faster in LLNL-G3Dv3 (Figure 13). The high-velocity anomalies near the core-mantle boundary are observed in GyPSuM, but are more detailed and intensified in the current model (Figure 12). Most global tomography models show prominent high-velocity anomalies in the deepest mantle centered beneath East Asia and the Americas. Several additional fast anomalies are seen along a linear trend beneath the Pacific Ocean to Central America apparently surrounding the Pacific superplume anomalies. Similar anomalies are seen in other global P-wave models [e.g. *van der Hilst et al*. 1997; *Bijwaard et al*., 1998; *Boschi and Dziewonski*, 1999; *Zhao* 2001], but are not prominent in all P-wave models partly owing to the limited resolution beneath the Pacific Ocean. The fast anomalies in the deep mantle may be attributed to ancient subducted slabs that have penetrated to the bottom of the mantle [*Richards and Engebretson*, 1992]. Moreover, it seems plausible that past subduction has led to the initial development of the superplumes by sweeping compositionally distinct material into piles which retain heat [*McNamara and Zhong*, 2005]. Thus the locations and geometry of both the high- and low-velocity anomalies near the base of the mantle may be intrinsically linked. Although the simulations presented in *McNamara and Zhong* [2005] demonstrate this possibility, it is unclear if the expected historic subduction since the Mesozoic could explain the actual geometries of the large fast and slow anomalies in the deep mantle. Aside from these large-scale processes, it is likely that a number of additional processes including phase transitions and melting contribute to our seismological observations of the deep mantle. See *Lay and Garnero* [2011] and *Tackley* [2012] for recent reviews.

From an interpretation standpoint, we observe mostly minor changes relative to the GyPSuM lower mantle model (Figure 13), particularly from 1600 km depth to the top of the D'' layer. The fact that overall patterns do not change suggests that the GyPSuM lower mantle model is largely consistent with the P-wave data considered in the current study. The consistency of GyPSuM and LLNL-G3Dv3 in the lower mantle provides confidence that our overall approach described in this study is valid. Further detailed interpretations of the resulting image will be reserved for future studies specifically focused on the geologic and geodynamic implications of structures observed in the LLNL-G3Dv3 model.

4.6 Data Fits

The LLNL-G3Dv3 model fits the ~2.8 million P-wave arrivals with an overall standard deviation of 0.96 seconds. This equates to 64% variance reduction relative to the initial event locations and travel time residuals with respect to the ak135 model (Figure 3). The overall level of data fit is better than many global P-wave studies, but similar to the fits obtained in *Bijwaard et al*. [1998] who considered a large number of P and Pn arrivals and lesser amounts of other P-wave phases. However, there are several factors that differ between the *Bijwaard et al*. [1998] study and the current study. Namely, although the previous tomographic study had fewer overall free model parameters in the inversion, the model cell spacing was allowed to be as small as 0.6° in the upper mantle where data were dense, compared to a uniform 1° node-based parameterization in the current study. In addition, the inversion performed in the *Bijwaard et al*. [1998] study included event location terms, event origin time terms, and station static terms as additional free parameters. Event and station terms effectively allow for the absorption of travel time signals due to very local structure around events and stations, thus allowing for higher degrees of data fit. Although the approach presented in *Bijwaard et al*. [1998] is perfectly valid, we note that these additional terms were not included within our inversion since we use a sophisticated multiple-event inversion approach prior to inversion and we chose to force the model to absorb as much travel time residual signal as possible.

P-wave arrivals at intermediate distances (15-23°) are the most difficult to reconcile with a 1-D model (Figure 3). At these distances, the 3-D ray paths are often quite different from 1-D ray paths (Figure 5) and the seismic waves may travel through large, intense regional structures thus accumulating travel time residual signals along the entire path. The LLNL-G3Dv3 model dramatically improves the level of fit to P-waves recorded at these intermediate distances, but these arrivals are still the least well reconciled compared to regional and teleseismic distances.

5. Single-Event Locations Versus Multiple-Event Locations

Knowledge of the location of past seismic events used to develop tomography models is a classical problem, and is of particular importance when designing a model that allows for accurate prediction of future event locations. In this study, we address the event location problem by adjusting the initial event locations with the global Bayesloc multiple-event relocation process prior to tomographic inversion. In the following sections, we describe an alternative imaging approach to understand the importance of our relocation procedures.

5.1 Procedures, Data Misfits and Location Comparison

In our alternative approach, we bypass the global Bayesloc multiple-event relocation process described in Section 3.1. Therefore, we begin the imaging process assuming the initial event locations. The initial event locations were determined on an individual basis using Bayesloc in single-event mode, without the aid of multiple-event constraints. We will further refer to the initial locations as Single-Event Locations or ‘SELs’. Similarly, we will refer to the multiple-event locations used to create LLNL-G3Dv3 as ‘MELs’. The only difference between the SELs and MELs datasets are that the residual travel times are computed using different event locations.

Identical to the procedures described in previous sections, we constructed a roughness versus misfit trade-off curve to estimate the appropriate damping weights (Figure 8). It is immediately evident that the same level of fit obtained using the MELs is impossible to achieve with the SELs with the same number of free parameters. This observation holds even when no damping constraints are used in the tomographic inversion. With a damping weight that balances misfit and image roughness, the root-mean-squared (RMS) misfit of the SELs data is 1.47 seconds compared to 0.96 seconds using the MELs. It should also be noted that the image produced using the SELs data is more than 2 times rougher, suggesting that a much more complex model is required to explain the data when these event locations are assumed.

After generating a tomographic model with the SELs data, we relocated the events in single-event mode using the newly generated tomographic model. The median epicenter shift was found to be 7.2 km which compares well to the multiple-event relocations to acquire the MELs (6.8 km). The new SELs also tend to move in the direction of the MELs. To demonstrate this behavior, we computed the parallel and normal components of SELs relocation vectors relative to the MELs relocation vectors and mapped out the occurrences (Figure 18). Since we must normalize by the MELs relocation shift for this analysis, we only included events that moved by at least 3 km in the multiple-event relocation process to form the relative relocation distributions. In Figure 18, the initial locations (SELs) are plotted at the origin. If all of the relocated SELs were co-located with the MELs, all events would plot at (1, 0). We find that the mode of the occurrences is at 0.70 in the direction of the MELs and -0.10 normal to the MELs. It is evident from this analysis that the SELs tend to move in direction of the MELs, but there exists a substantial spread in the distribution.

With these adjusted SELs, we performed tomographic inversion again. Not surprisingly, the new event locations allow for improved data fit relative to the initial SELs (Figure 8, red curves). However, with these adjusted locations, the misfit is still substantially greater than when the MELs are assumed. One might expect that, given the reduction of misfit after one event relocation, another round of relocation will further improve the data misfit. It might also be expected that the event locations will eventually converge to the MELs since the SELs generally moved in the direction of the MELs after the first iteration. However, we find very little improvement in the level of misfit after a 2nd relocation/tomography cycle (Figure 8, green line). Also, the mode of the relative relocation distribution does not significantly change from the first relocation distribution (Figure 18). Given these results, there is no clear indication that the SELs will converge with the MELs using this iterative process.

It is apparent that we can achieve higher levels of data fit with the multiple-event locations (MELs), suggesting that these locations are superior to the single-event locations (SELs) even after adjusting the SELs with an iterative relocation process. To further quantify the robustness of the MELs, we performed an additional Bayesloc multiple-event relocation process on the basis of the LLNL-G3Dv3 model. We find that the median shift in event epicenter was 2.7 km compared to the initial 6.8 km obtained in the original multiple-event relocation. The events tend to move randomly about the original MELs (opposed to regionally dependent systematic shifts) and form a tight relative relocation distribution (Figure 18). This implies that the epicenters determined through the Bayesloc multiple-event relocation process do not strongly depend on the underlying velocity model and iterative relocation is unnecessary.

It is commonly understood that seismic event location predictions are often biased to the underlying model used to determine them. In the context of our alternative procedures to iteratively invert and relocate, we effectively “burn in” the first 3-D model after we relocate the events. Thus, the 2nd round of relocation yields very little misfit improvement and the resulting model does not dramatically change from the 3-D model produced with the initial SELs. This phenomenon was recently confirmed in the study by *Valentine and Woodhouse* [2010] who demonstrated that an imprint of the model used to determine event locations will remain after tomographic inversion. It follows that, if the initial locations are incorrect, it is difficult to recover the correct tomographic model with simple iterative tomography/relocation procedures. Moreover, if the tomographic model is incorrect, event locations may never converge to the correct locations with an iterative relocation/tomography approach.

5.2 Image and Travel Time Prediction Comparisons

The tomographic image produced with the relocated single-event locations (referred to as the ‘SEL model’) differs from the LLNL-G3Dv3 model produced with multiple-event locations (MELs). The differences are most notable in the shallow upper mantle and transition zone (Figures 19-20). The differences between the tomographic models often appear subtle when comparing images side-by-side; but closer inspection reveals a number of local velocity anomalies that form spikes in the SEL model. These local velocity variations are clearly evident when mapping the difference between the LLNL-G3Dv3 and SEL models (Figures 19-20). We interpret many of the localized velocity spikes as artifacts resulting from event mislocation and/or origin time errors. Many of the spikes could be mitigated by introducing event terms in the inversion; however we note that our goal is to determine the correct timing and location of events prior to inversion and that event terms were also not included in the inversion process to obtain LLNL-G3Dv3. Although the iterative inversion/relocation process described in the previous section effectively reduced the overall complexity of the SEL model, the model remains more complicated than LLNL-G3Dv3.

In addition to the localized spikes observed in the SEL model, we observe more substantial differences between the two models. In particular, fast anomalies along the India-Eurasia collision zone vary significantly between the two models. In the LLNL-G3Dv3 model, a linear fast velocity anomaly is visible along the entire southern margin of the Tibetan Plateau in the shallow upper mantle (Figure 19). This anomaly, possibly representing underthrusted Indian lithosphere, is less intense overall and does not track the full extent of the Tibetan Plateau in the SEL model. A similar observation can be made in the transition zone beneath the Tibetan Plateau region where the SEL model depicts a more complicated set of anomalies than LLNL-G3Dv3 (Figure 20).

We find that fast slab anomalies in the shallow upper mantle (<250 km depth) are often more broad and intense in the SEL model. These effects are most notable along the northwestern Pacific margin, Central America, the Atlantic-Caribbean margin, and South America (Figure 19). Based on this observation alone, it might be implied that the SEL model is a better representation of subducted slab anomalies since they appear brighter at these depths. However, the SEL model is slower than LLNL-G3Dv3 in the deep upper mantle and transition zone beneath the same regions. A clear example of this behavior can be seen ~450 km beneath central Mexico where the Cocos slab is evident in the LLNL-G3Dv3 model, but missing in the SEL model (Figure 20).

Although the SEL and LLNL-G3Dv3 models appear remarkably similar in map view overall, these details are not inconsequential from an interpretation standpoint. For example, the

Cocos slab and the deeper Farallon anomaly appear to be a single continuous structure beneath the northern edge of the Caribbean plate in the LLNL-G3Dv3 model (Figure 21). The SEL model depicts a very different configuration, namely the Cocos plate appears faster and broader in the shallow mantle and is disconnected from the ancient Farallon remnant in the transition zone and lower mantle.

Although it is not known which model most closely resembles the actual Earth, it is clear that the SEL and LLNL-G3Dv3 models are distinctly different. For the purposes of this study, one of our primary concerns is how each of the models predicts travel times. Therefore, we computed direct P-wave travel times for each of the 3-D models (SEL and LLNL-G3Dv3 models) to understand how the velocity differences translate to travel time prediction differences. Specifically, travel times were computed on a grid of hypothetical events up to 90° from selected seismic stations including: i) ANMO in Albuquerque, New Mexico, ii) LPAZ in La Paz, Bolivia, iii) RAYN in Ar Rayn, Saudi Arabia, and iv) MAJO in Matsushiro, Japan (Figures 22-25).

Travel time residuals often reach ±4 seconds relative to the 1-D ak135 model at regional and intermediate distances (up to ~23° degrees). The patterns of travel time residuals at these distances are manifestations of the regional tectonic environment and often depict circular rings with sharp breaks in the patterns at distances corresponding to transition zone triplication crossover points. A particularly intense ringed pattern may be observed around station ANMO from western Canada to southern Mexico (Figure 22). The intensity of this particular ringed anomaly is due to the constructive affects of the low-velocity upper mantle beneath the source and receiver regions (Figure 11) and the deepened “410” km discontinuity to ~425 km along the paths [*Lawrence and Shearer*, 2008]. Travel time residuals relative to ak135 are typically within the range of ±2 seconds at teleseismic distances, but exceeded in some cases such as for North American events recorded at station LPAZ (Figure 23). It is important to note that these ranges of predicted travel time residuals are in good agreement with the distribution of the actual data (see Figure 3).

In our selected examples, the largest regional/intermediate travel time residuals occur for hypothetical events recorded at station MAJO in Japan (Figure 25). For events in China and the Korean Peninsula, P-waves recorded at MAJO are predicted to arrive very late relative to ak135 predictions due to the large low-velocity mantle wedge illustrated in Figure 5. For hypothetical events occurring east of MAJO, P-waves arrive early due to the combination of thin crust, subducting slab and relatively old oceanic lithosphere east of Japan.

Although the two 3-D velocity models often produce fairly similar travel time residual patterns overall, there still are marked differences in the predicted travel times. The differences between the LLNL-G3Dv3 and SEL model travel times often exceed 50% of the difference relative to the ak135 model. More specifically, we find that the differences in travel times predicted by the two 3-D models can be 2 seconds or more at regional/intermediate distances (compared to ~4 seconds relative to ak135) and 1 second or more at teleseismic distances (compared to ~2 seconds relative to ak135). These residual travel time patterns and intensities are important for location determinations; the fact that the patterns are different suggests that each 3-D model will predict different locations for future seismic events. A comprehensive follow-up study exploring this assertion is currently underway.

6. Summary and Conclusions

In this paper, we describe the development of a global-scale P-wave tomography model called LLNL-G3Dv3. The model is designed within a hierarchical tessellation framework that explicitly contains aspherical Earth structure, including multiple undulating layers in the crust and upper mantle. We employ a 3-D ray tracing approach that includes multi-pathing and demonstrate the importance of 3-D ray tracing for modeling regional seismic data. Tomographic inversion is performed with a multi-scale inversion approach called PMTI that captures regional structural trends as well as finer details where data allow without designing an irregular mesh [see *Simmons et al.*, 2011].

The LLNL-G3Dv3 model depicts many geologically and geodynamically significant structures described in the text. From an interpretation standpoint, many of the structures seen in LLNL-G3Dv3 are similar those seen in other global P-wave models, when compared collectively. Some of the more intriguing features observed in the current model are the apparent slab anomalies in the transition zone beneath much of Eurasia. These slab anomalies tend to be broader, with sharper velocity gradients along the edges, and higher amplitude than most other P-wave models. Within this network of fast anomalies, we detect a large high-velocity anomaly in the transition zone extending from the India-Eurasia collision zone to Mongolia. This anomaly spans the entire Tibetan Plateau and suggests that much of the subducted slab material associated with the closing of the Tethys Oceans may be trapped in the transition zone beneath western China. If this anomaly is indeed a massive subducted slab remnant, it contributes significantly to the estimated budget of tomographically identified subducted slab volumes associated with the collision [e.g. *Hafkenscheid et al.*, 2006].

The locations of the seismic events used to develop LLNL-G3Dv3 were determined prior to tomographic inversion with the algorithm called Bayesloc. Bayesloc is a seismic location algorithm that simultaneously models the entire multiple-event system using a Bayesian methodology [see *Myers et al.* 2007, 2009, 2011]. Bayesloc was modified in this study to include regional travel time curve adjustments to account for more localized structural trends.

We compared the multiple-event locations (locations used to determine LLNL-G3Dv3) with single-event locations (SELs) determined without the benefit of multiple-event constraints. We employed a classical iterative technique to invert for velocity structure and subsequently relocate the SELs to produce a comparison image and determine if similar locations could be obtained. We find that the relocated SELs generally move toward the multiple-event locations, but typically never converge. Moreover, we find that the relocated SELs produce a more complex model and that the data misfit is higher than when the multiple-event locations are assumed. This observation suggests that the multiple-event locations are more internally consistent.

Although the LLNL-G3Dv3 and SEL models are generally similar, the detailed differences are substantial in terms of predicted travel times. Travel time prediction differences can be 2 seconds or more at regional and intermediate distances, and on the order of 1 second at teleseismic distances. For perspective, the difference between the travel times predicted with the two 3-D models is 50% of the difference relative to the ak135 1-D model in some cases. Clearly, if the models predict different travel times, each will yield different location predictions for future events. It is therefore extremely important to have accurate locations of events prior to tomographic inversion, particularly if the resulting image is to be used for locating future events.

The overall goal of our global imaging research is to enhance seismic event monitoring, particularly seismic event location determination. Preliminary seismic event location prediction validation tests using the LLNL-G3Dv3 model show considerable location improvements relative to a 1-D model (on the order of 30-60% median mis-location improvement). A comprehensive validation study is currently underway and will be the subject of an upcoming paper.

Acknowledgments

This work performed under the auspices of the U.S. Department of Energy by Lawrence Livermore National Laboratory under Contract DE-AC52-07NA27344. LLNL-JRNL-?

References

Alessandrini, B. (1989), The hydrostatic equilibrium figure of the Earth: and iterative approach, *Phys. Earth Planet. Int.*, *54*, 180-192.

Antolik, M., Y. J. Gu, G. Ekström and A. M. Dziewonski (2003), J362D28: a new joint model of compressional and shear velocity in the Earth's mantle, *Geophys. J. Int.*, *153*, 443-466.

Badro, J., G. Fiquet, F. Guyot, J. -P. Rueff, V. V. Struzhkin, G. Vankó, and G. Monaco (2003), Iron partitioning in Earth's mantle: Toward a deep lower mantle discontinuity, *Science*, *300*, 789–791.

Badro, J., J. -P. Rueff, G. Vankó, G. Monaco, G. Fiquet, and F. Guyot (2004), Electronic transitions in perovskite: Possible nonconvecting layers in the lower mantle, *Science*, *305*, 383–386.

Ballard, S., J. R. Hipp and C. J. Young (2009), Efficient and accurate calculation of ray theory seismic travel time through variable resolution 3D Earth models, *Seis. Res. Lett.*, *80*(6), 990-1000.

Bassin, C., G. Laske and G. Masters (2000), The current limits of resolution for surface wave tomography in North America, *EOS Trans*. AGU, *81*, F897.

Baumgardner, J. R. and P. O. Frederickson (1985), Icosahedral discretization of the two-sphere, *SIAM J. Numer. Anal.*, *22*(6), 1107-1115.

Behn, M. D., C. P. Conrad, and P. G. Silver (2004), Detection of upper mantle flow associated with the African superplume, *Earth Planet. Sci. Lett*., *224*, 259-274.

Bijwaard, H., W. Spakman and E. R. Engdahl (1998), Closing the gap between regional and global travel time tomography, *J. Geophys. Res*., *103(B12)*, 30,055-30,078.

Bondár, I., S. C. Myers, E. R. Engdahl, and E. A. Bergman (2004), Epicenter accuracy based on seismic network criteria, *Geophys. J. Int*., *156*, 483–496, doi:10.1111/j.1365-246X.2004.02070.x.

Bondár, I., and K. L. McLaughlin (2009), A new ground truth data set for seismic studies, *Seismol. Res. Lett*., *80*, 465–472, doi:10.1785/gssrl.80.3.465.

Boschi, L. and A. M. Dziewonski (1999), High- and low-resolution images of the Earth’s mantle: implications of different approaches to tomographic modeling, *J. Geophys. Res*., *104*(B11), 25567-25594.

Chiao, L. -Y. and B. -Y. Kuo (2001), Multiscale seismic tomography, *Geophys. J. Int*., *145*, 517-527.

Constable, C. G., R. L. Parker and P. B. Stark (1993), Geomagnetic field models incorporating frozen-flux constraints, *Geophys. J. Int.*, *113*, 419-433.

Creager, K. C., and T. M. Boyed (1992), Effects of earthquake mislocation on estimates of velocity structure, *Phys. Earth Planet. Inter*., *75*, 63-76, doi:10.1016/0031-9201(92)90118-F.

Crowhurst, J. C., J. M. Brown, A. F. Goncharov, and S. D. Jacobsen (2009), Elasticity of (Mg,Fe)O through the spin transition of iron in the lower mantle, *Science*, *319*, 451–453.

Deuss, A. (2009), Global observations of mantle discontinuities using SS and PP precursors, *Surv. Geophys*., *30*, 301-326.

Engdahl, E. R., R. van der Hilst and R. Buland (1998), Global teleseismic earthquake relocation with improved travel times and procedures for depth determination, *Bull. Seis. Soc. Amer*., *88*(3), 722-743.

Flanagan, M. P. and P. M. Shearer (1998), Global mapping of topography on transition zone velocity discontinuities by stacking of SS precursors, *J. Geophys. Res*., *103*(B2), 2673-2692.

Forte, A. M., S. Quéré, R. Moucha, N. A. Simmons, S. P. Grand, J. X. Mitrovica, and D. B. Rowley (2010), Joint seismic-geodynamic-mineral physical modeling of African geodynamics: A reconciliation of deep mantle convection with surface geophysical constraints, Earth Planet. Sci. Lett., 295, 329–341.

Fukao, Y., M. Obayashi, H. Inoue and M. Nenbai (1992), Subducting slabs stagnant in the mantle transition zone, *J. Geophys. Res*., *97*, B4, 4809-4822.

Fukao, Y., S. Widiyantoro and M. Obayashi (2001), Stagnant slabs in the upper and lower mantle transition region, *Rev. Geophys*., *39*, 291-323.

Fukao, Y., A. To and M. Obayashi (2003), Whole mantle P tomography using P and PP-P data, *J. Geophys. Res*., *108*(B1), doi: 10.1029/2001JB000989.

Grand, S. P., R. D. Van der Hilst and S. Widiyantoro (1997), Global seismic tomography: a snapshot of convection in the Earth, *GSA Today*, *7*, 1-7.

Gung, Y., Y. -T. Hsu, L. -Y. Chiao and M. Obayashi (2009), Multiscale waveform tomography with two-step parametermization, *J. Geophys. Res*., *114*, doi: 10.1029/2008JB006275.

Gurnis, M., J. X. Mitrovica, J. Ritsema, and H.-J. van Heijst (2000), Constraining mantle density structure using geological evidence of surface uplift rates: The case of the African Superplume, Geochem. Geophys. Geosyst., 1(7), doi:10.1029/1999GC000035.

Gurrola, H. and J. B. Minster (1998), Thickness estimates of the upper-mantle transition zone from bootstrapped velocity spectrum stacks of receiver functions, *Geophys. J. Int*., *133*, 31-43.

Hafkenscheid, E., M. J. R. Worte and W. Spakman (2006), Subduction history of the Tethyan region derived from seismic tomography and tectonic reconstructions, *J. Geophys. Res*., *111*, B08401, doi: 10.1029/2005JB003791.

Hofmeister, A. M. (2006), Is low-spin Fe^{2+} present in Earth's mantle?, *Earth Planet. Sci. Lett*., *243*, 44–52.

Houser, C., G. Masters, P. Shearer and G. Laske (2008), Shear and compressional velocity models of the mantle from cluster analysis of long-period waveforms, *Geophys. J. Int*., *174*, 195-212.

Ishii, M. and J. Tromp (1999), Normal-mode and free-air gravity constraints on lateral variations in velocity and density of Earth's mantle, *Science*, *285*(5431), 1231-1236.

Ishii, M. and A. M. Dziewonski (2002), The innermost inner core of the Earth: Evidence for a change in anisotropic behavior at the radius of about 300 km, *PNAS*, *99*(22), 14026-14030.

Kárason, H. & R. D. van der Hilst (2000), Constraints on mantle convection from seismic tomography, in: M. R. Richards, M. R. Gordon, R. D. van der Hilst (Eds.), The History and Dynamics of Global Plate Motion, AGU, Washington, DC, pp. 277-288.

Kennett, B. L. N., E. R. Engdahl and R. Buland (1995), Constraints on seismic velocities in the Earth from travel times, *Geophys. J. Int*., *122*, 108-124.

Kennett, B. L. N., S. Widiyantoro, and R. D. van der Hilst (1998), Joint seismic tomography for bulk sound and shear wave speed in the Earth's mantle, J. Geophys. Res., 103(B6), 12,469–12,493, doi:10.1029/98JB00150.

Lawrence, J. G. and P. M. Shearer (2008), Imaging mantle transition zone thickness with *SdS-SS* finite-frequency sensitivity kernels, *Geophys. J. Int*., *174*, 143-158.

Lawson, C. L. (1984), C^1 surface interpolation for scattered data on a sphere, *J. Mathematics*, *14*(1), 177-202.

Lay, T., and E. J. Garnero (2011), Deep mantle seismic modeling and imaging, *Ann. Rev. Earth Planet. Sci.*, *39*, 91-123, doi:10.1146/annurev-earth-040610-133354.

Li, C., R. D. van der Hilst, E. R. Engdahl and S. Burdick (2008), A new global model for P wave speed variations in Earth's mantle, *Geochem. Geophys. Geosys*., *9*(5), doi: 10.1029/2007GC001806.

Lin, J.-F., G. Vankó, S. D. Jacobsen, V. Iota, V. V. Struzhkin, V. V. Prakapenka, A. Kuznetsov, and C.-S. Yoo (2007), Spin transition zone in Earth's lower mantle, *Science*, *317*, 1740–1743.

Lin, J.-F., H. Watson, G. Vankó, E. E. Alp, V. V. Prakapenka, P. Dera, V. V. Struzhkin, A. Kubo, J. Zhao, C. McCammon, and W. J. Evans (2008), Intermediate-spin ferrous iron in lowermost mantle postperovskite and perovskite, *Nat. Geosci*., *1*, 688–691.

Lithgow-Bertelloni, C., and P. G. Silver (1998), Dynamic topography, plate driving forces and the African superswell, *Nature*, *395*(6699), 269-272.

Masters, G., G. Laske, H. Bolton & A. M. Dziewonski (2000), The relative behavior of shear velocity, bulk sound speed, and compressional velocity in the mantle: implications for chemical and thermal structure, *in Earth's Deep Interior: Mineral Physics and*

Tomography from the Atomic to the Global Scale, edited by S. -I. Karato et al., pp. 63-87, AGU, Washington, DC.

McCammon, C., I. Kantor, O. Narygina, J. Rouquette, U. Ponkratz, I. Sergueev, M. Mezouar, V. Prakapenka, and L. Dubrovinsky (2008), Stable intermediate- spin ferrous iron in lower mantle perovskite, *Nat. Geosci*., *1*, 684–687.

McNamara, A. K., and S. Zhong (2005), Thermochemical structures beneath Africa and the Pacific Ocean, *Nature*, *437*(7062), 1136– 1139.

Myers, S. C., G. Johannesson and W. Hanley (2007), A Bayesian hierarchical method for multiple-event seismic location, *Geophys. J. Int*., *171*, 1049-1063.

Myers, S. C., G. Johannesson and W. Hanley (2009), Incorporation of probabilistic seismic phase labels into a Bayesian multiple-event seismic locator, *Geophys. J. Int*., *177*, 193-204.

Myers, S. C., M. L. Begnaud, S. Ballard, M. E. Pasyanos, W. S. Phillips, A. L. Ramirez, M. S. Antolik, K. D. Hutchenson, J. J. Dwyer, C. A. Rowe and G. S. Wagner (2010), A crust and upper-mantle model of Eurasia and North Africa for P_n travel-time calculation, *Bull. Seis. Soc. Amer*., *100*(2), 640-656.

Myers, S. C., G. Johannesson and N. A. Simmons (2011), Global-scale P-wave tomography optimized for prediction of teleseismic and regional travel times for Middle East events: 1. Data set development, *J. Geophys. Res.*, *116*, B04304, doi:10.1029/2010JB007967.

Nakiboglu, S. M. (1982), Hydrostatic theory of the Earth and its mechanical implications, *Phys. Earth Planet. Int*., *28*, 302-311.

Ni, S. D., E. Tan, M. Gurnis, and D. V. Helmberger (2002), Sharp sides to the African superplume, *Science*, *296*(5574), 1850–1852.

Nyblade, A. A. and S. W. Robinson (1994), The African superswell, *Geophys. Res. Lett*., *21*(9), 765-768.

Obayashi, M., T. Sakurai and Y. Fukao (1997), Comparison of recent tomographic models. In *Proc. Int. Symp. on New Images of the Earth's Interior Through Long Term Ocean-Floor Observations, Earthquake Research Institute, University of Tokyo, Tokyo, Japan* (ed. K. Suyehiro).

Pasyanos, M. E., W. R. Walter, M. P. Flanagan, P. Goldstein and J. Bhattacharyya (2004), Building and testing an a priori geophysical model for Western Eurasia and North Africa, *Pure Appl. Geophys*., *161*, 235-281.

Peter, D., C. Tape, L. Boschi and J. H. Woodhouse (2007), Surface wave tomography: global membrane waves and adjoint methods, *Geophys. J. Int*., *171*, 1098-1117, doi:10.1111/j.1365-246X.2007.03554.x.

Richards, M. A., and D. C. Engebretson (1992), Large-scale mantle convection and the history of subduction, *Nature*, *355*, 437-440.

Ritsema, J., S. Ni and D. V. Helmberger (1998), Evidence for strong shear velocity reductions and velocity gradients in the lower mantle beneath Africa, *Geophys. Res. Lett*., *25*(23), 4245-4248.

Ruppert, S., D., Dodge, A. Elliott, M. Ganzberger, T. Hauk and E. Matzel (2005), Enhancing seismic calibration research through software automation and scientific information management, in *Proceedings of the 27th Seismic Research Review: Ground-Based Nuclear Explosion Monitoring Technologies,* LA-UR-05-6407, Vol. 2.

Sambridge, M. and R. Faletič (2003), Adaptive whole Earth tomography, *Geochem. Geophys. Geosys*., *4*(3), doi:10.1029/2001GC000213.

Simmons, N. A., A. M. Forte and S. P. Grand (2006), Constraining mantle flow with seismic and geodynamic data: a joint approach, *Earth Planet. Sci. Lett*. *246*, 109–124.

Simmons, N. A., A. M. Forte and S. P. Grand (2007), Thermochemical structure and dynamics of the African superplume, *Geophys. Res. Lett., 34*(2), L02301, doi: 10.1029/2006GL028009.

Simmons, N. A., A. M. Forte and S. P. Grand (2009), Joint seismic, geodynamic and mineral physical constraints on three-dimensional mantle heterogeneity: implications for the relative importance of thermal versus compositional heterogeneity, *Geophys. J. Int*. *177*(5), 1284–1304.

Simmons, N. A., A. M. Forte, L. Boschi and S. P. Grand (2010), GyPSuM: A joint tomographic model of mantle density and seismic wave speeds, *J. Geophys. Res*., *115*, B12310, doi:10.1029/2010JB007631.

Simmons, N. A., S. C. Myers, and G. Johannesson (2011), Global-scale P wave tomography optimized for prediction of teleseismic and regional travel times for Middle East events: 2. Tomographic inversion, *J. Geophys. Res*., *116*, B04305, doi:10.1029/2010JB007969.

Speziale, S., V. E. Lee, S. M. Clark, J.- F. Lin, M. P. Pasternak, and R. Jeanloz (2007), Effects of Fe spin transition on the elasticity of (Mg,Fe)O magnesiowüstites and implications for the seismological properties of the Earth's lower mantle, *J. Geophys. Res*., *112*, B10212, doi:10.1029/2006JB004730.

Stackhouse, S., J. P. Brodholt, and G. D. Price (2007), Electronic spin transitions in iron-bearing MgSiO3 perovskite, *Earth Planet. Sci. Lett*., *253*, 282–290.

Steck, L. K., C. A. Rowe, M. L. Begnaud, W. S. Phillips, V. L. Gee and A. A. Velasco (2004), Advancing seismic event location through difference constraints and three-dimensional models, *Proceedings of the 26th Seismic Research Review*, Orlando, Florida, September 2004.

Stockmann, R. C. C. Finlay and A. Jackson (2009), Imaging Earth's crustal magnetic field with satellite data: a regularized spherical triangle tessellation approach, *Geophys. J. Int*., *179*, 929-944.

Su, W., and A. M. Dziewonski (1997), Simultaneous inversion for 3-D variations in shear and bulk velocity in the mantle, *Phys. Earth Planet. Inter*., *100*(1–4), 135–156.

Sun, D., D. Helmberger and M. Gurnis (2010), A narrow, mid-mantle plume below southern Africa, *Geophys. Res. Lett*., *37*, L09302, doi:10.1029/2009GL042339.

Tackley, P. J. (2012), Dynamics and evolution of the deep mantle resulting from thermal, chemical, phase and melting effects, *Earth-Sci. Rev*., *110*, 1-25.

Tan, E., and M. Gurnis (2005), Metastable superplumes and mantle compressibility, *Geophys. Res. Lett*., *32*, L20307, doi:10.1029/2005GL024190.

Torsvik, T. H., B. Steinberger, M. Gurnis and C. Gaina (2010), Plate tectonics and net lithosphere rotation over the past 150 My, *Earth Planet. Sci. Lett*., *291*, 106-112.

Trampert, J., F. Deschamps, J. Resovsky and D. Yuen (2004), Probabilistic tomography maps chemical heterogeneities throughout the lower mantle, *Science*, *306*(5697), 853-856.

Um, J. and C. Thurber (1987), A fast algorithm for two-point seismic ray tracing, *Bull. Seis. Soc. Amer*., *77*, 972-986.

Valentine, A. P. and J. H. Woodhouse (2010), Reducing errors in seismic tomography: combined inversion for sources and structure, *Geophys. J. Int*., *180*, 847-857.

van der Hilst, R. D., S. Widiyantoro and E. R. Engdahl (1997), Evidence for deep mantle circulation from global tomography, *Nature*, *386*, 578-584.

Wang, Z. and F. A. Dahlen (1995), Spherical-spline parameterization of three-dimensional Earth models, *Geophys. Res. Lett*., *22*(22), 3099-3102.

Wentzcovitch, R. M., J. F. Justo, Z. Wu, C. R. S. da Silva, D. A. Yuen, and D. Kohlstedt (2009), Anomalous compressibility of ferropericlase throughout the iron spin cross-over, *Proc. Natl. Acad. Sci*., *106*(21), 8447–8452.

Woods, M. T., and G. F. Davies (1982), Late Cretaceous genesis of the Kula plate, *Earth Planet. Sci. Lett*., *58*, 161-166.

Zhao, D., A. Hasegawa, and S. Horiuchi (1992), Tomographic imaging of P and S wave velocity structure beneath northeastern Japan, *J. Geophys. Res*., *97*, 19909–19928.

Zhao, D. (2001), Seismic structure and origin of hotspots and mantle plumes, *Earth Planet. Sci. Lett. 192*, 251-265.

Zhao, D. and J. Lei (2004), Seismic ray path variations in a 3D global velocity model, *Phys. Earth Planet. Int*., *141*, 153-166.

Zhou, H. -W. (1996), A high-resolution *P* wave model for the top 1200 km of the mantle, *J. Geophys. Res.*, *101*(B12), 27791-27810.

Figure Captions

Figure 1. Examples of event clusters formed during the Bayesloc multiple-event relocation process. Red circles are the 4 example target events and dark blue circles are events that are members of each cluster. Light blue circles mark events not used to form any of the example clusters. An event cluster is formed for each event based on the criteria described in the text and Bayesloc [Myers et al., 2007, 2009] is used to relocate each cluster.

Figure 2. Bayesloc multiple-event relocation vectors. The red circles mark the epicenter locations determined one event at a time (single-event locations). Arrows illustrate the epicenter shifts due to multiple-event relocation using the clustering technique described in the text. The median epicenter shift if 6.8 km and there are clear regional trends, particularly along subduction zones where the locations tend to move trenchward. Note that the length of the arrows are amplified for illustrative purposes, thus the end of the arrows do not represent the new locations.

Figure 3. Data fits for the ~2.8 million P and Pn arrivals used for tomography. The left column illustrates residual travel times as a function of distance. The travel time residual occurrences are expressed in terms of the log of the density and the values are normalized at each distance to have a maximum value of 1. The column on the right illustrates residual travel times binned by distance with 3 different statistics: median residual (red lines), mean of the absolute value of the residuals (green lines), and the standard deviation (blue lines). Each row represents different combinations of assumed event locations and models used to predict the travel time (as indicated).

Figure 4. Summary of the LLNL-G3Dv3 model architecture. a) Selected levels of the spherical tessellation grids that define the location of nodes in the lateral extent. Nodes are placed at arbitrary radii in the direction of geocentric vectors pointing from the center of the Earth to the vertices. This hierarchical model structure is exploited in the PMTI imaging technique [see *Simmons et al*., 2011]. b) Description of the model layers. Wavy lines correspond to layers that undulate and thick lines correspond to double layers needed to honor discontinuities. Flat lines correspond to layers that do not undulate, but note that all layers conform to the expected hydrostatic shape of the Earth (none of the layers are spherical). The maximum lateral resolution in the upper mantle is ~1° (nodes defined by the Level 7 tessellation grid). The maximum lateral resolution in the lower mantle is ~2° (nodes defined by the Level 6 tessellation grid).

Figure 5. A comparison of 1-D and 3-D ray paths for an event 20 km beneath the Japan region. The 1-D ray paths (black lines) were computed with the ak135 model and the 3-D ray paths (green lines) were computed with the LLNL-G3Dv3 model (illustrated in the background). The minimum-time ray paths tend to focus into the subducted slab (blue anomalies) and tend to avoid the very slow mantle wedge structure (red anomalies). The discrepancy between the 1-D and 3-D paths is most significant at regional and intermediate distances.

Figure 6. Depth resolution of the inversion models at all stages of the PMTI imaging process. Layers in the full model (defined on the left) are combined in the inversion and the number of inversion layers increases with tessellation levels that define the lateral resolution. The yellow

bars indicate the span of layers combined to form a single inversion layer where an average slowness perturbation is determined. The layers in the crust are always combined in the inversion; therefore the entire crustal stack is adjusted at each lateral node.

Figure 7. Flowchart of the inversion process. Three-dimensional ray paths are computed and the full PMTI process is performed multiple times to account for the interdependence of ray paths and velocity structure. Ray paths produced with an intermediate model ('Raytracing Model') are mapped into the starting model to determine travel time residuals relative to the starting model. Therefore slowness perturbations determined with the PMTI process are always with respect to the starting model to reduce artifacts referred to as *ghost anomalies*. See the text for further explanation.

Figure 8. Roughness versus data misfit for a spectrum of damping weights and four sets of event locations. Solid symbols mark models that provide a reasonable balance of model complexity and data misfit for each set of event locations. Bayesloc Multiple-event Location Data = Travel time residuals based on locations produced through a Bayesian process that models the full multiple-event system; Single-event Location Data = Travel time residuals based on locations determined without the multiple-event constraints. The Bayesloc Multiple-event Locations yield models (blue line with circles) that predict the data better and with a less complicated model than the Single-event Locations (red line with circles). We generated a tomographic model with the Single-event Location Data and relocated the events on the basis of the determined 3-D model (red line with squares), yielding a substantial reduction of data misfit.

This procedure was repeated yielding no substantial additional improvement (green line with triangles). Even with the iterative tomography/relocation process, the multiple-event locations yield less complicated and better-fitting models than the relocated single-event data.

Figure 9. Resolution tests with a complex input model. The input pattern (top left) is a checkerboard that combines long-wavelength regional trends embedded with finer details. The pattern is repeated with opposite signs in each model layer (top right). We show the recovery in the shallowest mantle layer (just below the Moho) and along one particular 360° cross section traced in green.

Figure 10. Checkerboard model recovery at 3 selected depths. (left column) The recovery of the multiple-layer synthetic model described in Figure 10. (right column) The recovery of checkerboard models defined at only a single layer (i.e. all synthetic checkerboard layers above and below the selected depths are set to zero).

Figure 11. The LLNL-G3Dv3 P-wave velocity model at selected depths in the upper mantle. Values are shown in absolute velocity (km/s) and percentage perturbations relative to the mean velocity are indicated in the bottom right of each panel. The tildes (~) indicate undulating layers and therefore the depth to each point may vary.

Figure 12. The LLNL-G3Dv3 P-wave velocity model at selected depths in the lower mantle. Values are shown in absolute velocity (km/s) and percentage perturbations relative to the mean velocity are indicated in the bottom right of each panel.

Figure 13. Differences between LLNL-G3Dv3 and the starting model at selected depths (LLNL-G3Dv3 minus the starting model).

Figure 14. Selected cross sections through the LLNL-G3Dv3 model showing structures beneath North America.

Figure 15. Selected cross sections through the LLNL-G3Dv3 model showing structures beneath South America.

Figure 16. Selected cross sections through the LLNL-G3Dv3 model showing structures beneath Africa and Eurasia.

Figure 17. Selected cross sections through the LLNL-G3Dv3 model showing structures beneath Indonesia and the northwestern Pacific convergent zones.

Figure 18. Epicenter relocations after tomography compared to initial (pre-tomography) Bayesloc multiple-event locations. (top left) New event locations (post-tomography) are plotted by comparing the directionality relative to the pre-tomography relocations and normalizing. The number of occurrences in a finite set of bins is determined to evaluate how the relocations on the basis of a 3-D model compare to the initial Bayesloc multiple-event locations. (top right) After performing tomography with the Bayesloc Multiple-event Location (MEL) data, events were relocated on the basis of the resulting 3-D model (i.e. LLNL-G3Dv3). The new event locations tend to cluster tightly around the original locations. (middle right) After performing tomography using the Single-Event Location (SEL) data, events were relocated on the basis of the resulting model. The events tend to move toward the multiple-event locations, but with a substantial spread (note the color scale differences for the panels in the right column). (bottom right) After performing another iteration of tomography/relocation without the aid of multiple-event constraints, the distribution tightens and the mode is ~70% in the direction of the initial MELs. (bottom left) Comparison of relocation distributions along the X-axis (in the direction of the initial MELs). Although the first round of tomography/relocation with SEL data resulted in epicenter locations more similar to the initial BELs, the 2nd round did not show promising signs of convergence to the same locations.

Figure 19. Comparison of models produced with the Multiple-Event Location (MEL) data and the Single-Event Location (SEL) data at 220 km depth.

Figure 20. Comparison of models produced with the Multiple-Event Location (MEL) data and the Single-Event Location (SEL) data at 450 km depth.

Figure 21. Comparison of models produced with the Multiple-Event Location (MEL) data and the Single-Event Location (SEL) data showing different images of the connectivity of the Cocos and Farallon plates.

Figure 22. Travel time residual patterns for times predicted with LLNL-G3Dv3 and the Single-Event Location model for events up to 90° from station ANMO in Albuquerque, New Mexico. (a, b) LLNL-G3Dv3 residuals relative to ak135; (c, d) Single-Event Location model residuals relative to ak135; (e, f) Travel time differences between the two 3-D models.

Figure 23. Travel time residual patterns for times predicted with LLNL-G3Dv3 and the Single-Event Location model for events up to 90° from station PAZ in La Paz, Bolivia. (a, b) LLNL-G3Dv3 residuals relative to ak135; (c, d) Single-Event Location model residuals relative to ak135; (e, f) Travel time differences between the two 3-D models.

Figure 24. Travel time residual patterns for times predicted with LLNL-G3Dv3 and the Single-Event Location model for events up to 90° from station RAYN in Ar Rayn, Saudi Arabia. (a, b) LLNL-G3Dv3 residuals relative to ak135; (c, d) Single-Event Location model residuals relative to ak135; (e, f) Travel time differences between the two 3-D models.

Figure 25. Travel time residual patterns for times predicted with LLNL-G3Dv3 and the Single-Event Location model for events up to 90° from station MAJO in Matsushiro, Japan. (a, b) LLNL-G3Dv3 residuals relative to ak135; (c, d) Single-Event Location model residuals relative to ak135; (e, f) Travel time differences between the two 3-D models.

Table 1: Travel time arrivals for input into Bayesloc multiple-event location

Phase	Number Input to Bayesloc	Number Used in tomography
P	2,662,081	2,553,180
Pn	286,297	266,882
pP	182,890	
Sn	80,912	
sP	78,696	
PcP	62,458	
Pg	30,911	
Lg	22,162	
Total	3,406,407	2,820,062

Table 2. Computational aspects of the PMTI imaging for the dataset considered.

Tessellation Recursion Level	Average Node Spacing (arc degrees)	Inversion Model Layers	Free Parameters	Sensitive Nodes per Datum‡	Matrix Size† (Gbytes)	Sparseness†† (%)	Inversion Time††† (mm:ss)
1	63	3	36	12	0.5	67.30	00:14
2	32	3	126	15	0.7	88.09	00:19
3	16	6	972	31	1.4	96.77	00:42
4	8	10	6,420	54	2.5	99.15	01:21
5	4	16	40,992	93	4.2	99.87	03:13
6	2	31	317,502	195	8.8	99.94	08:15
7¶	1¶	45	1,075,290	274	12.5	99.98	14:45
							Total: 28:49

‡The average number of non-zero elements in the tomographic sensitivity matrix per source-receiver pair. There are ≈2.8 million P and P_n observations in this particular dataset.

† Tomographic matrix is represented as a sparse matrix with components including ray path lengths (double precision) and row/column pointers (integers).

†† Sparseness is measured by the ratio of the number of null elements in the tomographic matrix and the number of elements in the full system of equations.

†††Benchmarks performed on a Dell R710 64-bit Linux Server using only a single 3 GHz processor. Inversions were performed with a MATLAB based LSQR algorithm (64 iterations per recursion level). The computation times include workspace memory allocation and the 'Total' time reflects the time to complete the PMTI inversion (tessellation levels 1-7).

¶ The highest resolution in the lower mantle is 2-degree spacing (tessellation recursion level 6). Only the upper mantle velocity structure is modeled at 1-degree resolution (level 7 recursion).

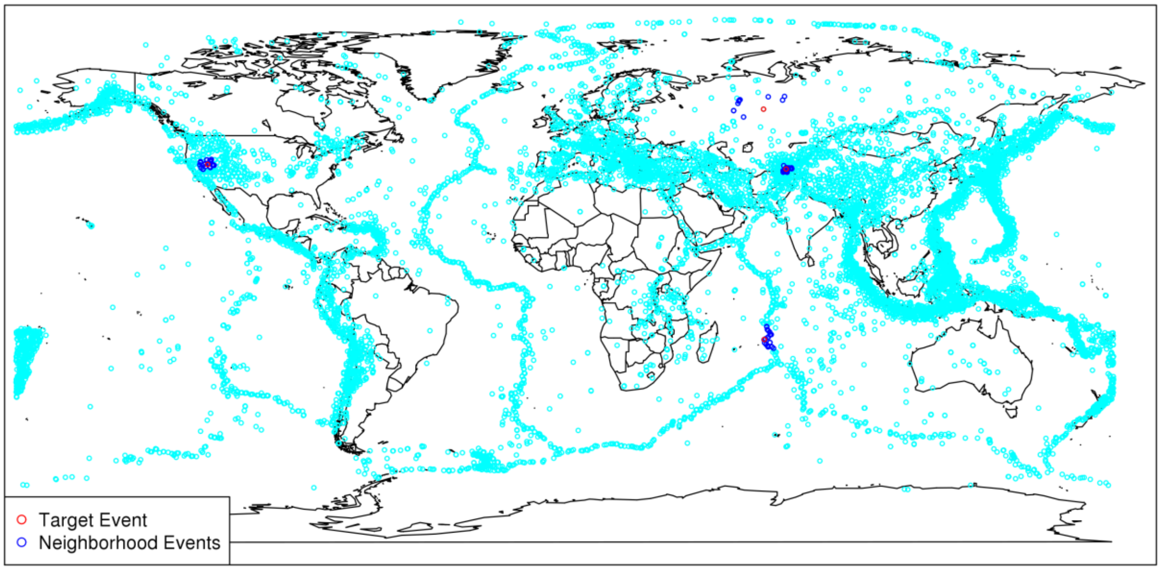

Figure 1

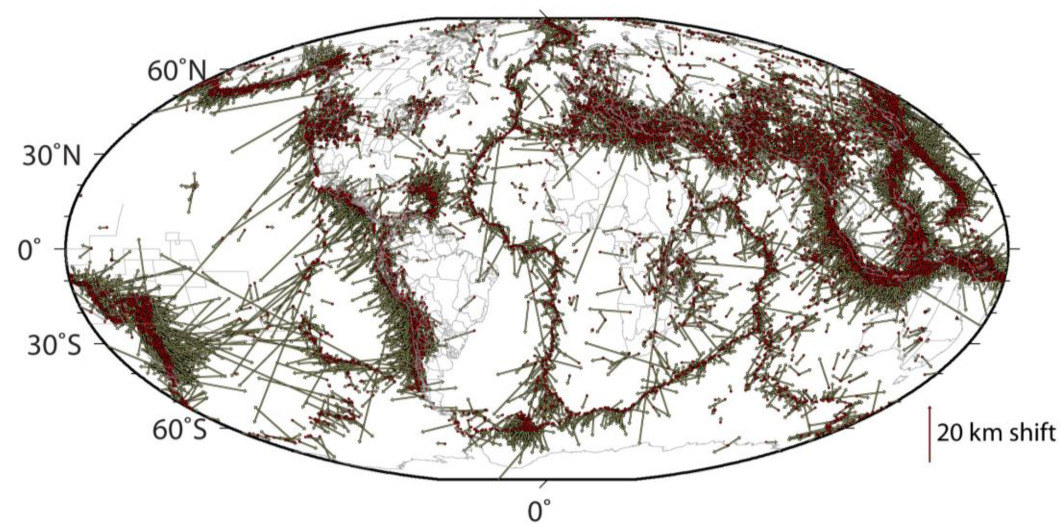

Figure 2

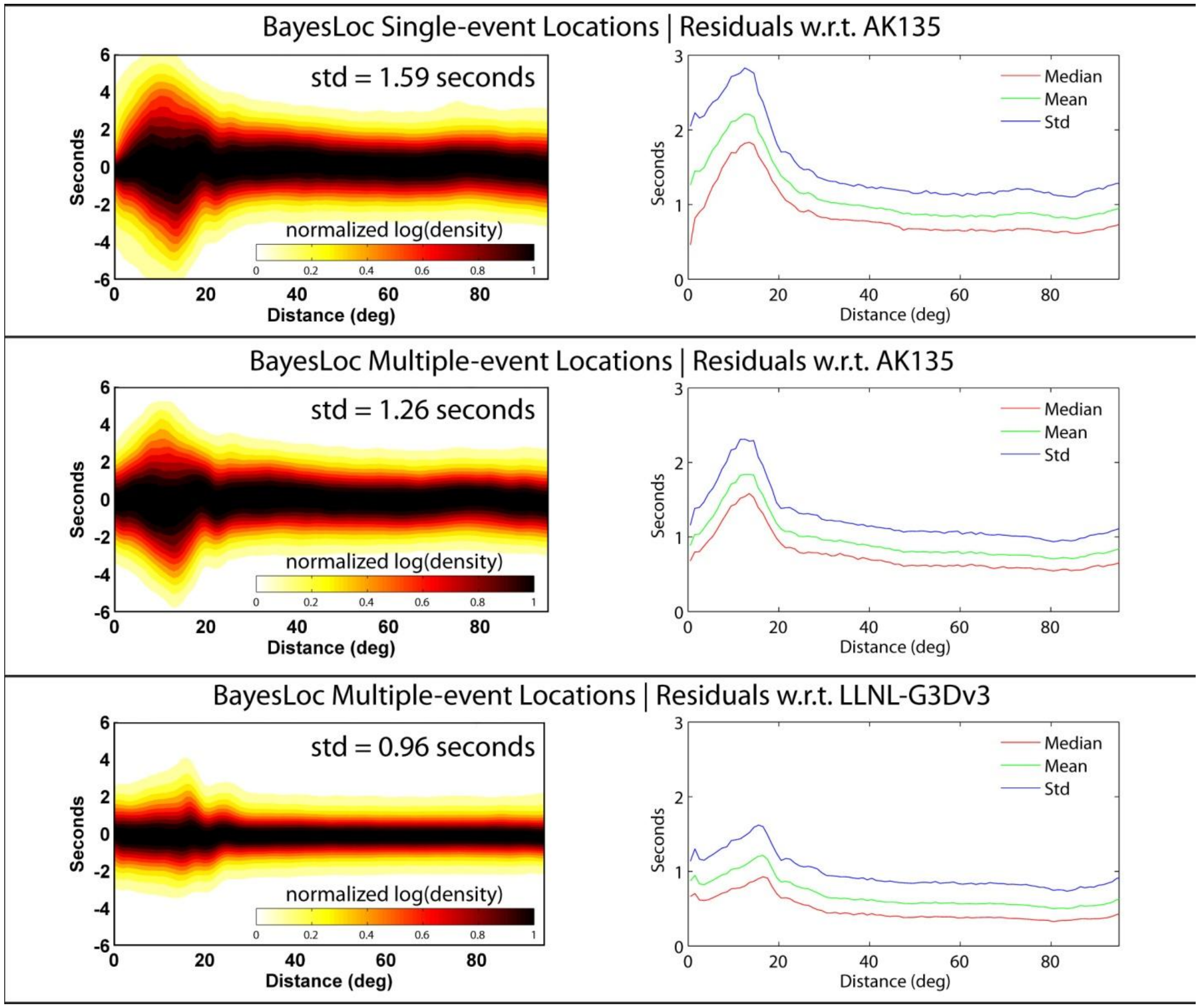
BayesLoc Single-event Locations | Residuals w.r.t. AK135
std = 1.59 seconds
normalized log(density)
Seconds
Distance (deg)
Median
Mean
Std
BayesLoc Multiple-event Locations | Residuals w.r.t. AK135
std = 1.26 seconds
BayesLoc Multiple-event Locations | Residuals w.r.t. LLNL-G3Dv3
std = 0.96 seconds

Figure 3

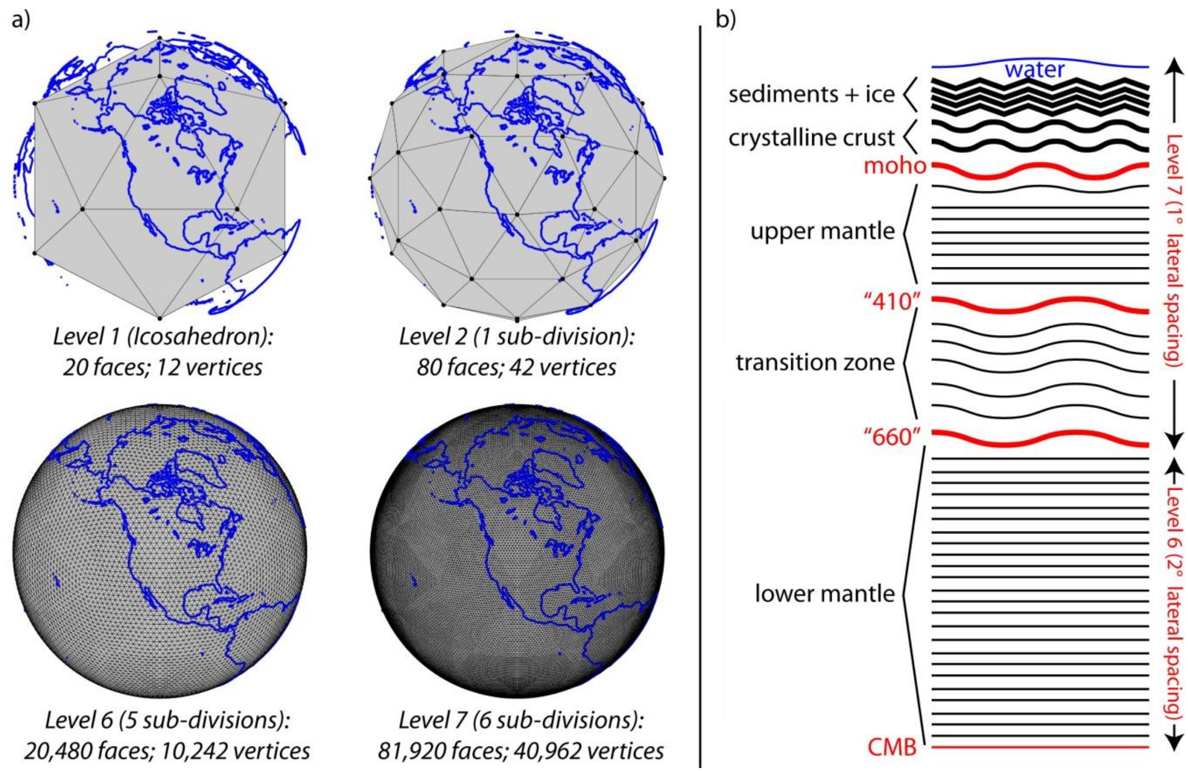

Figure 4: Model Architecture

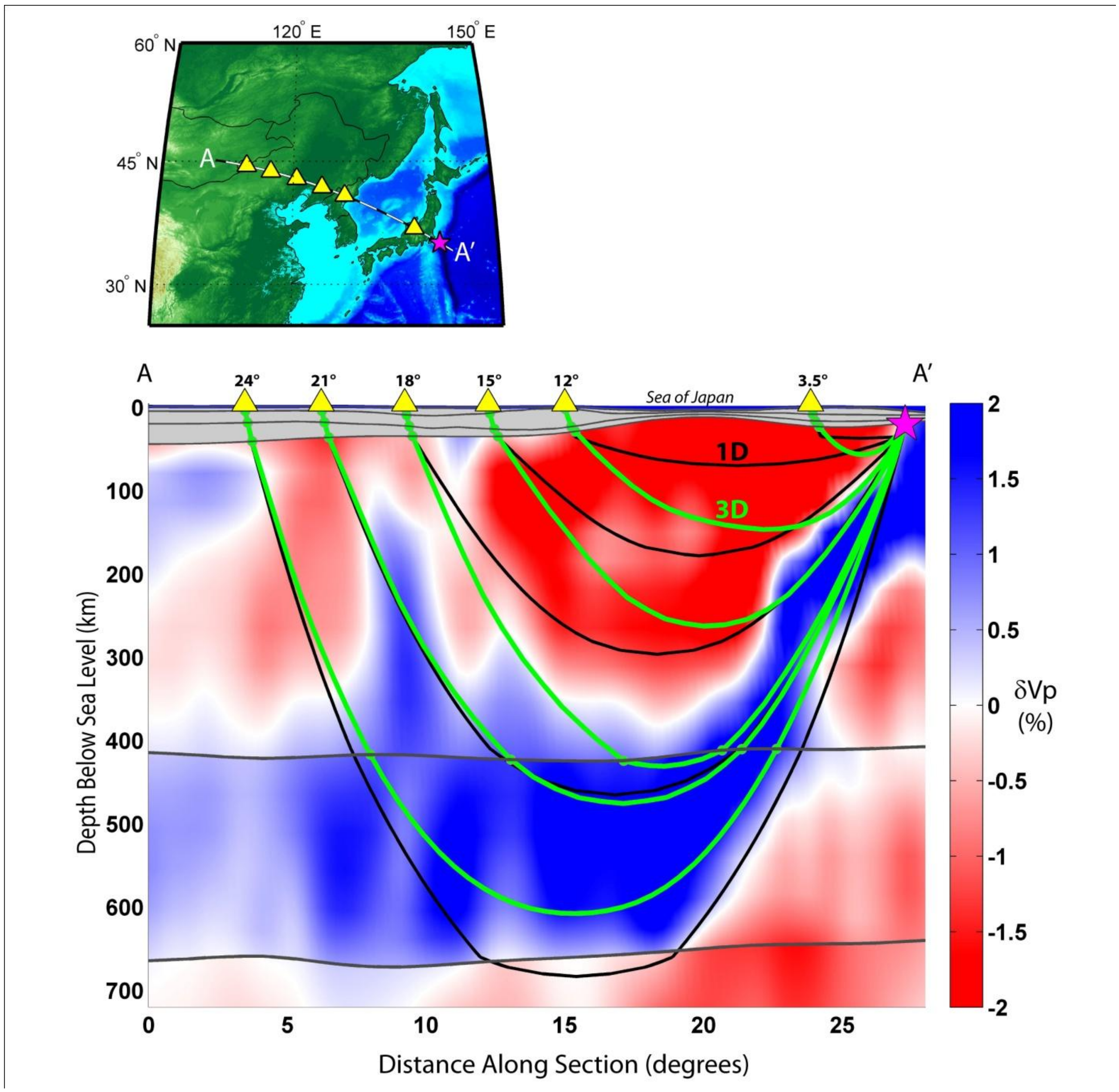
60° N
120° E
150° E
45° N
30° N
A
A′
24°
21°
18°
15°
12°
3.5°
Sea of Japan
1D
3D
Depth Below Sea Level (km)
0
100
200
300
400
500
600
700
0
5
10
15
20
25
Distance Along Section (degrees)
δVp (%)
2
1.5
1
0.5
0
-0.5
-1
-1.5
-2

Figure 5

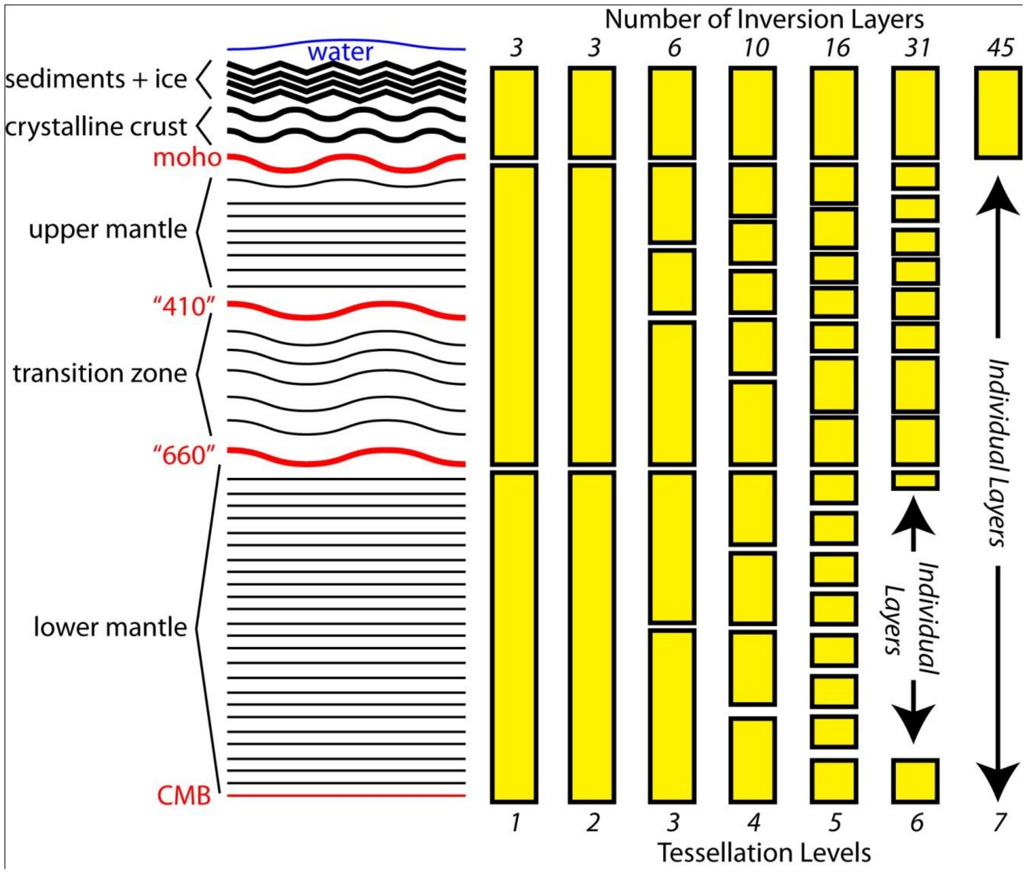
Number of Inversion Layers
3
3
6
10
16
31
45
water
sediments + ice
crystalline crust
moho
upper mantle
"410"
transition zone
"660"
lower mantle
CMB
Individual Layers
Individual Layers
1
2
3
4
5
6
7
Tessellation Levels

Figure 6:

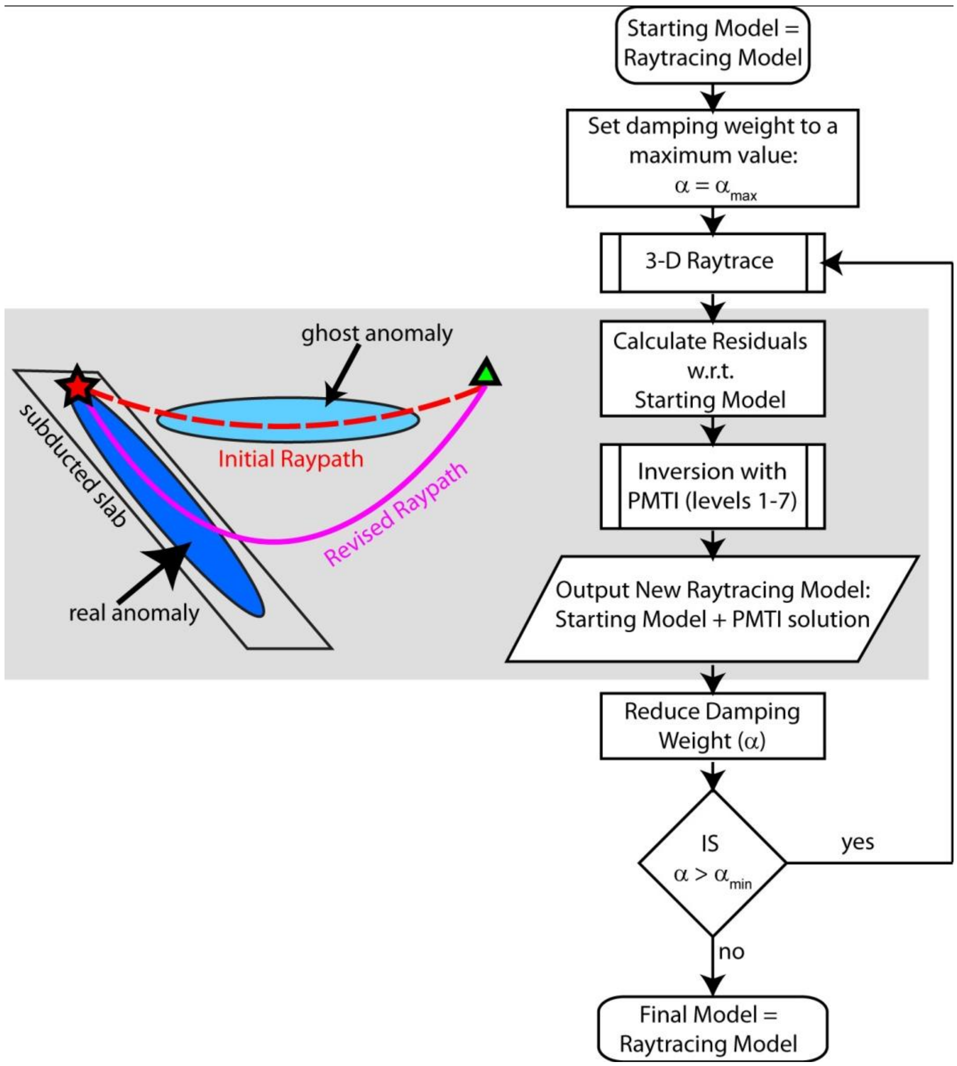
Starting Model =
Raytracing Model
Set damping weight to a
maximum value:
$\alpha = \alpha_{max}$
3-D Raytrace
Calculate Residuals
w.r.t.
Starting Model
Inversion with
PMTI (levels 1-7)
Output New Raytracing Model:
Starting Model + PMTI solution
Reduce Damping
Weight (α)
IS
$\alpha > \alpha_{min}$
yes
no
Final Model =
Raytracing Model
ghost anomaly
subducted slab
Initial Raypath
Revised Raypath
real anomaly

Figure 7

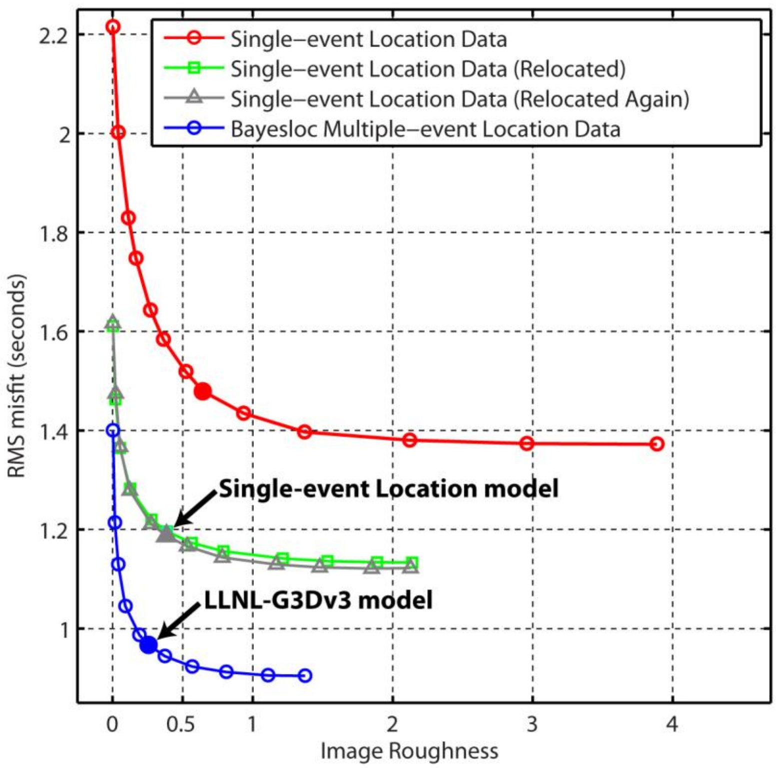
Single−event Location Data
Single−event Location Data (Relocated)
Single−event Location Data (Relocated Again)
Bayesloc Multiple−event Location Data
Single-event Location model
LLNL-G3Dv3 model
RMS misfit (seconds)
Image Roughness
2.2
2
1.8
1.6
1.4
1.2
1
0
0.5
1
2
3
4

Figure 8

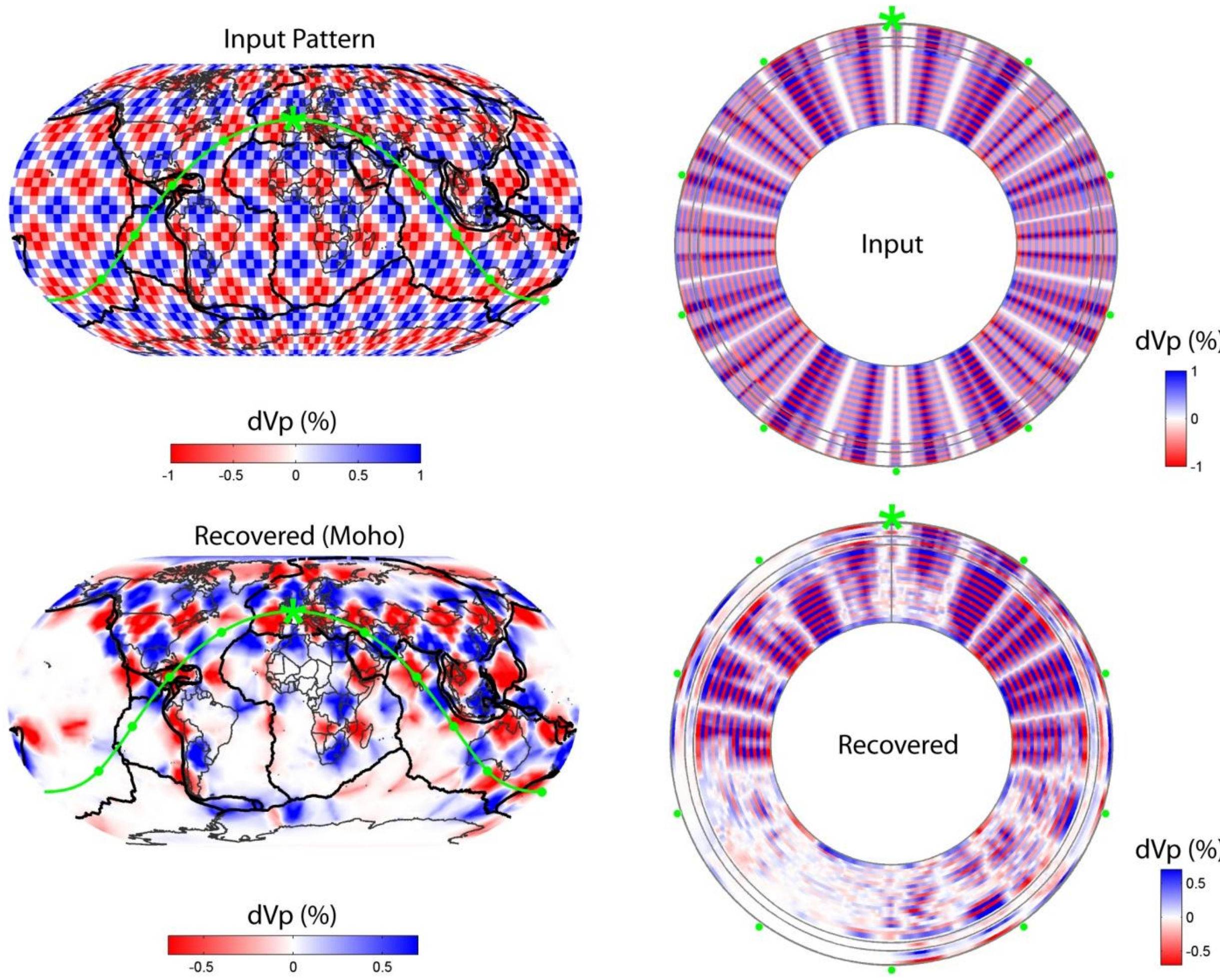
Input Pattern
dVp (%)
-1
-0.5
0
0.5
1
Input
dVp (%)
1
0
-1
Recovered (Moho)
dVp (%)
-0.5
0
0.5
Recovered
dVp (%)
0.5
0
-0.5

Figure 9

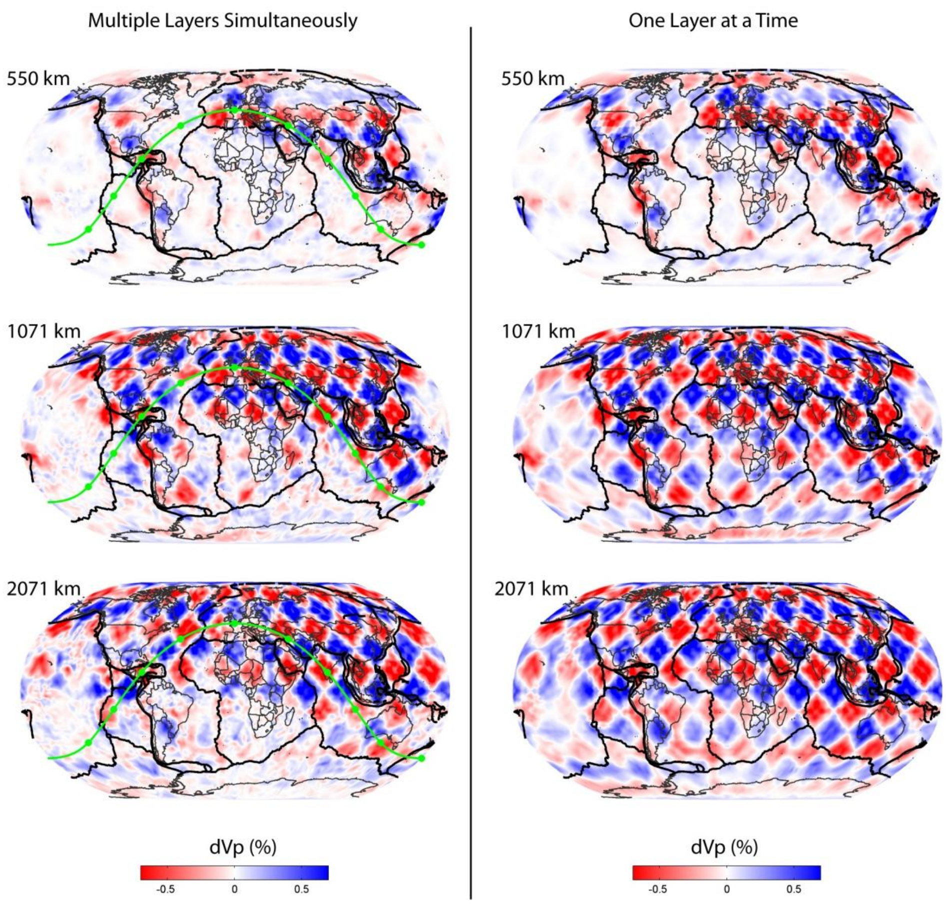
Multiple Layers Simultaneously
One Layer at a Time
550 km
1071 km
2071 km
550 km
1071 km
2071 km
dVp (%)
-0.5
0
0.5
dVp (%)
-0.5
0
0.5

Figure 10

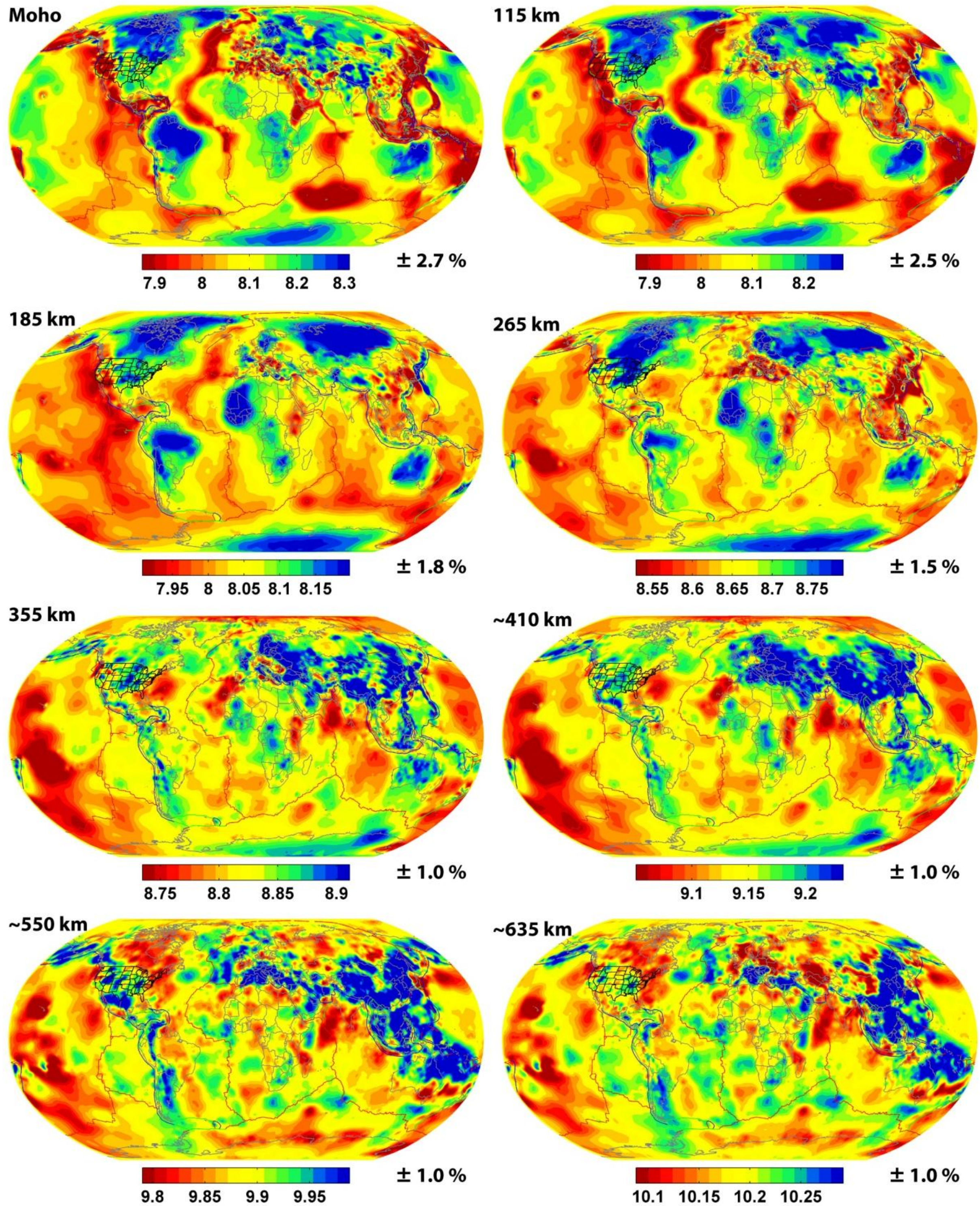
Moho
± 2.7 %
7.9 8 8.1 8.2 8.3
115 km
± 2.5 %
7.9 8 8.1 8.2
185 km
± 1.8 %
7.95 8 8.05 8.1 8.15
265 km
± 1.5 %
8.55 8.6 8.65 8.7 8.75
355 km
± 1.0 %
8.75 8.8 8.85 8.9
~410 km
± 1.0 %
9.1 9.15 9.2
~550 km
± 1.0 %
9.8 9.85 9.9 9.95
~635 km
± 1.0 %
10.1 10.15 10.2 10.25

Figure 11

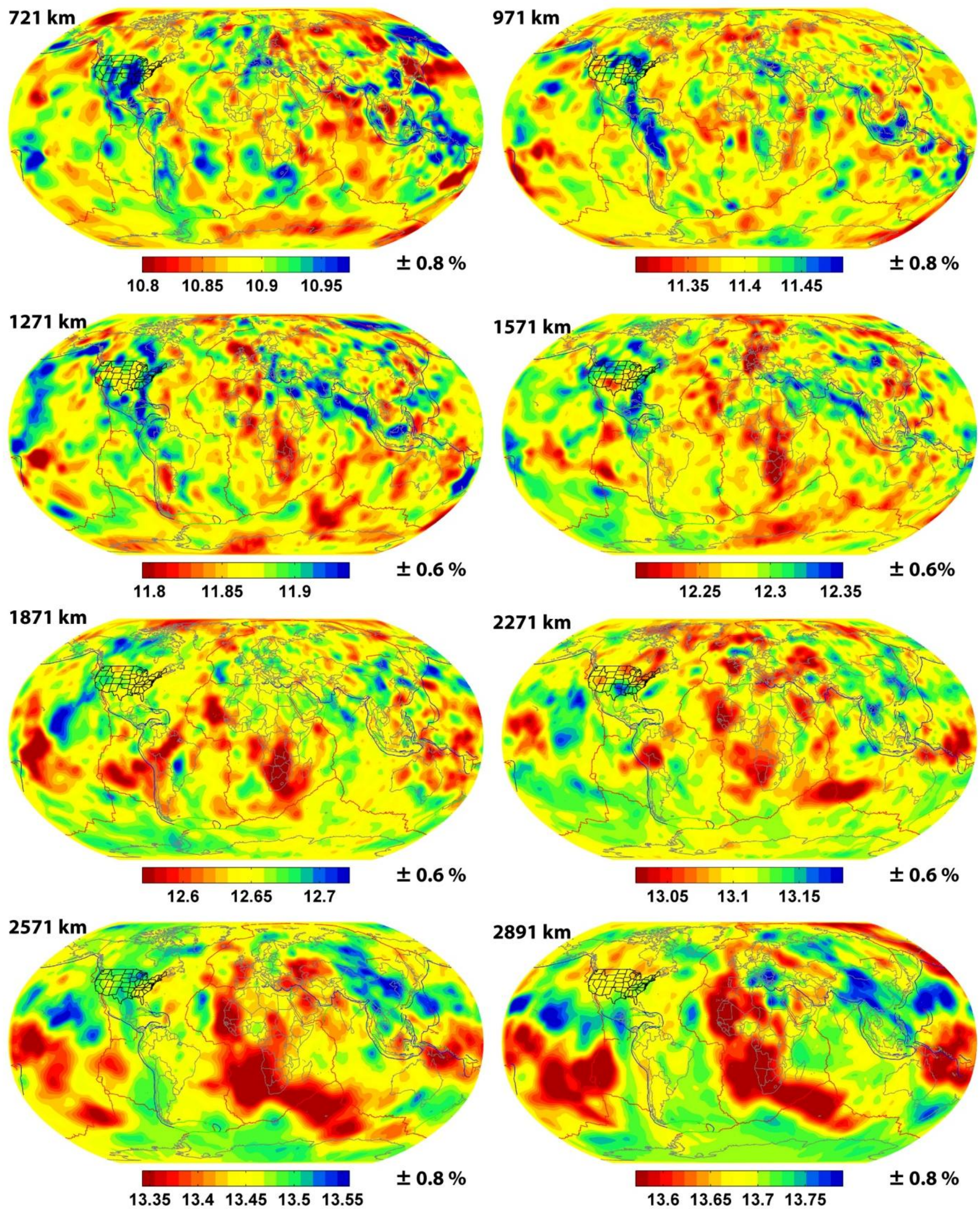
721 km
10.8 10.85 10.9 10.95
± 0.8 %
971 km
11.35 11.4 11.45
± 0.8 %
1271 km
11.8 11.85 11.9
± 0.6 %
1571 km
12.25 12.3 12.35
± 0.6%
1871 km
12.6 12.65 12.7
± 0.6 %
2271 km
13.05 13.1 13.15
± 0.6 %
2571 km
13.35 13.4 13.45 13.5 13.55
± 0.8 %
2891 km
13.6 13.65 13.7 13.75
± 0.8 %

Figure 12

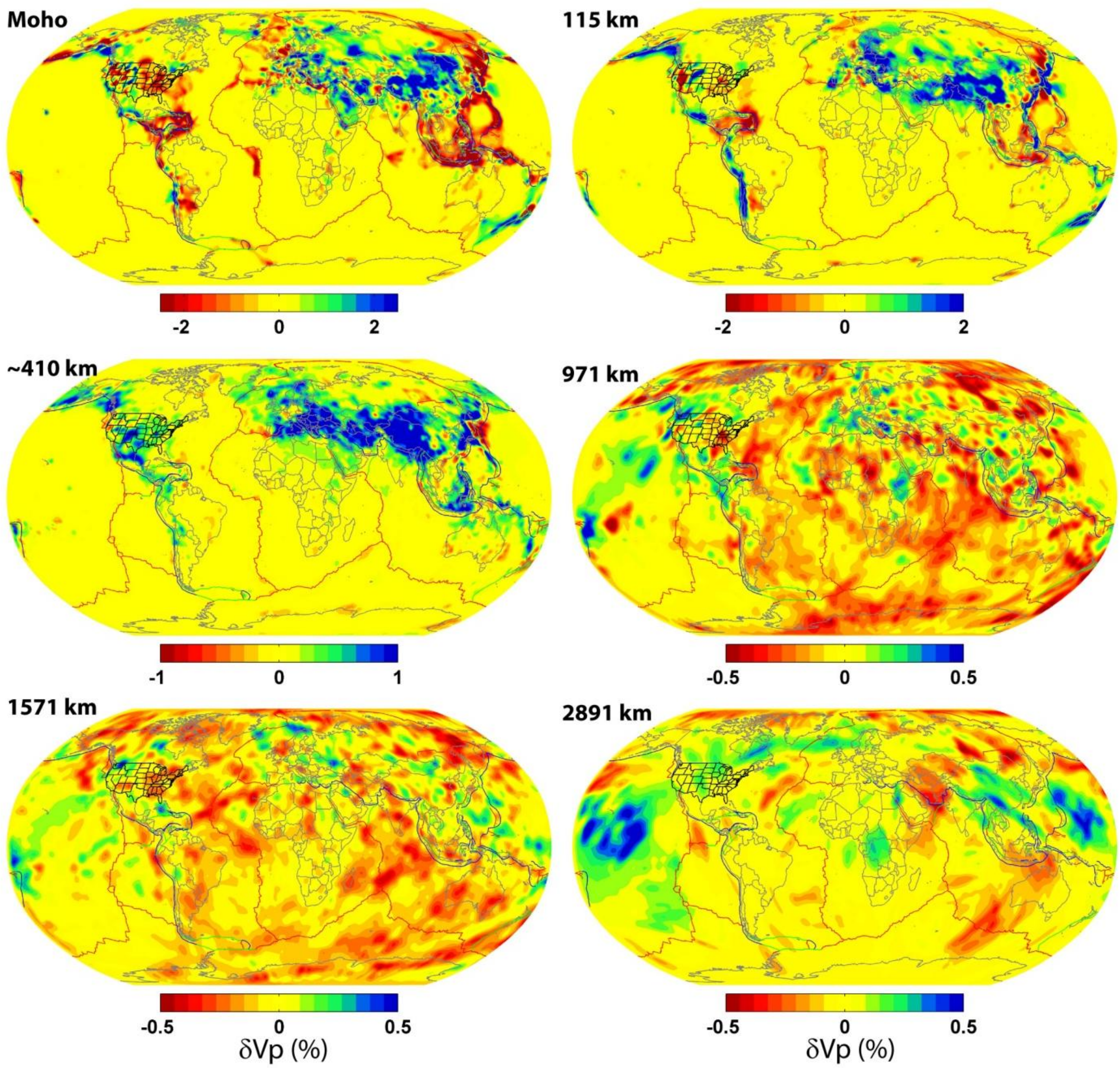

Figure 13: LLNL-G3Dv3 minus Starting Model

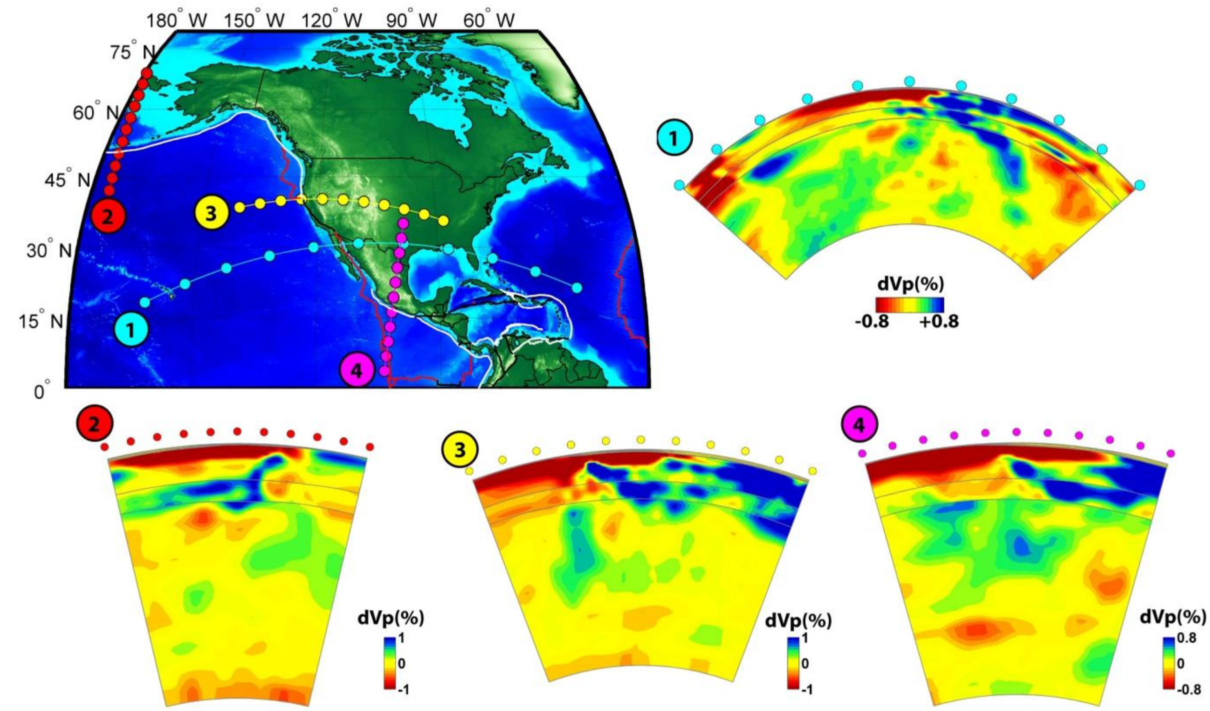

180° W
150° W
120° W
90° W
60° W
75° N
60° N
45° N
30° N
15° N
0°
1
2
3
4
dVp(%)
-0.8
+0.8
dVp(%)
1
0
-1
dVp(%)
1
0
-1
dVp(%)
0.8
0
-0.8

Figure 14

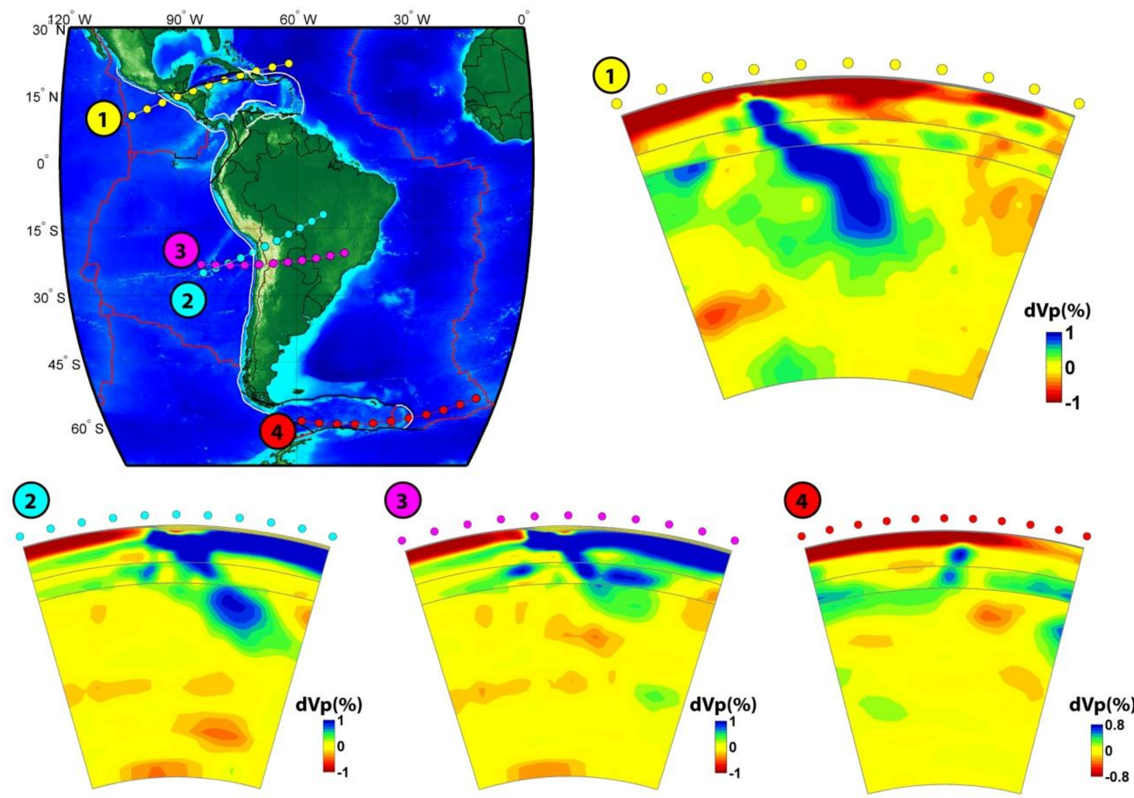
120° W
90° W
60° W
30° W
0°
30° N
15° N
0°
15° S
30° S
45° S
60° S
1
2
3
4
dVp(%)
1
0
-1
dVp(%)
1
0
-1
dVp(%)
1
0
-1
dVp(%)
0.8
0
-0.8

Figure 15

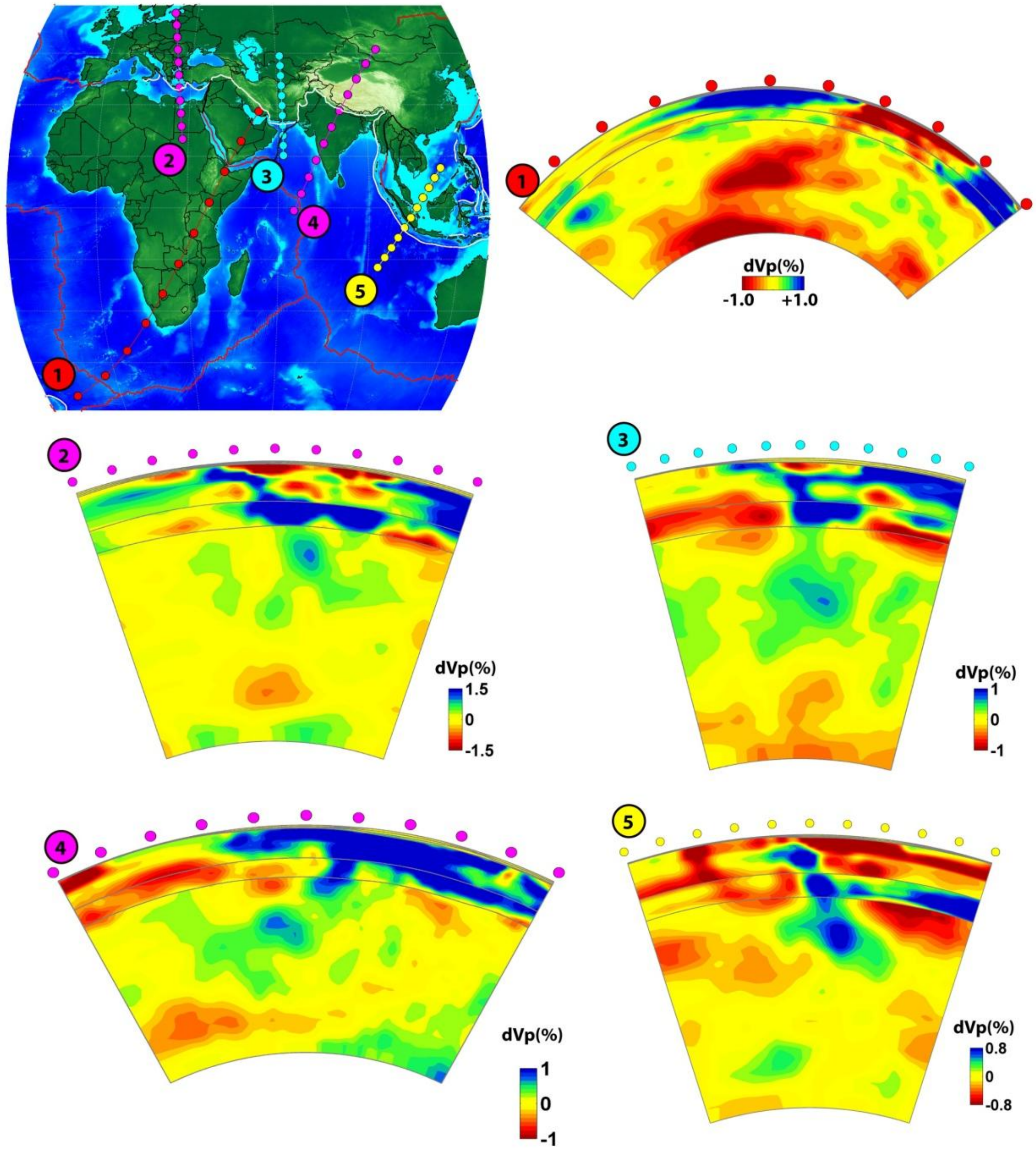

Figure 16

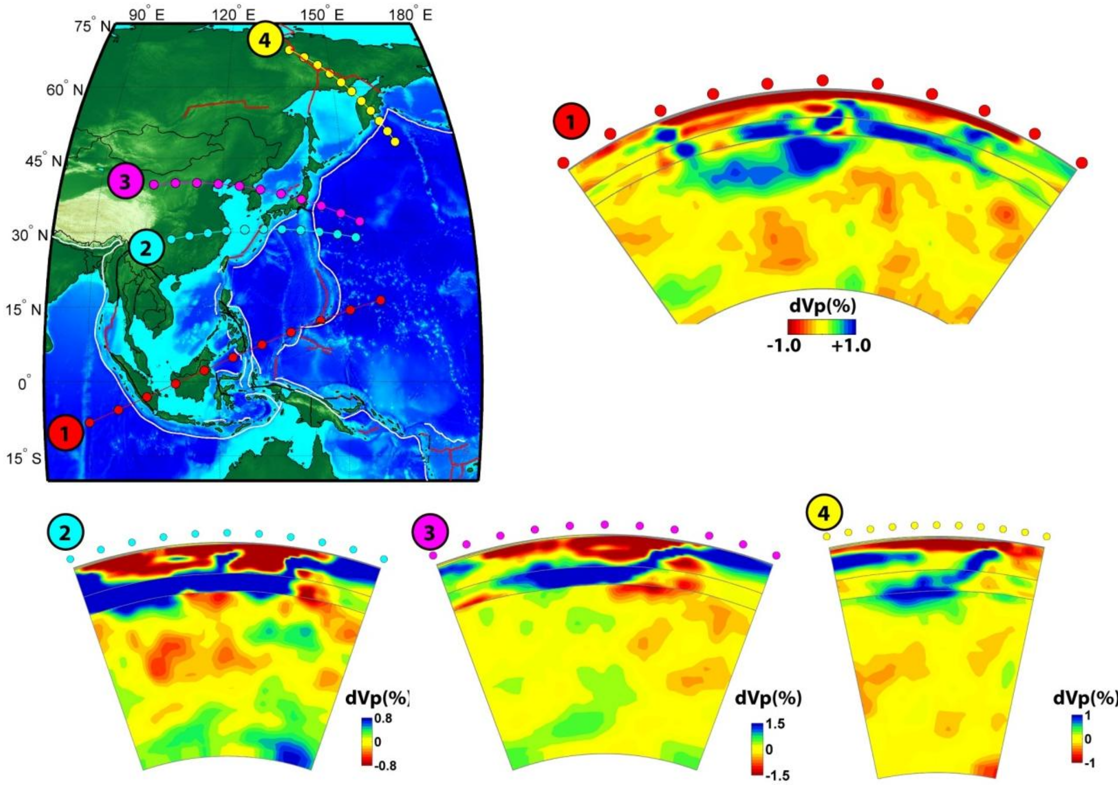
75° N
90° E
120° E
150° E
180° E
60° N
45° N
30° N
15° N
0°
15° S
1
2
3
4
dVp(%)
-1.0
+1.0
dVp(%)
0.8
0
-0.8
dVp(%)
1.5
0
-1.5
dVp(%)
1
0
-1

Figure 17

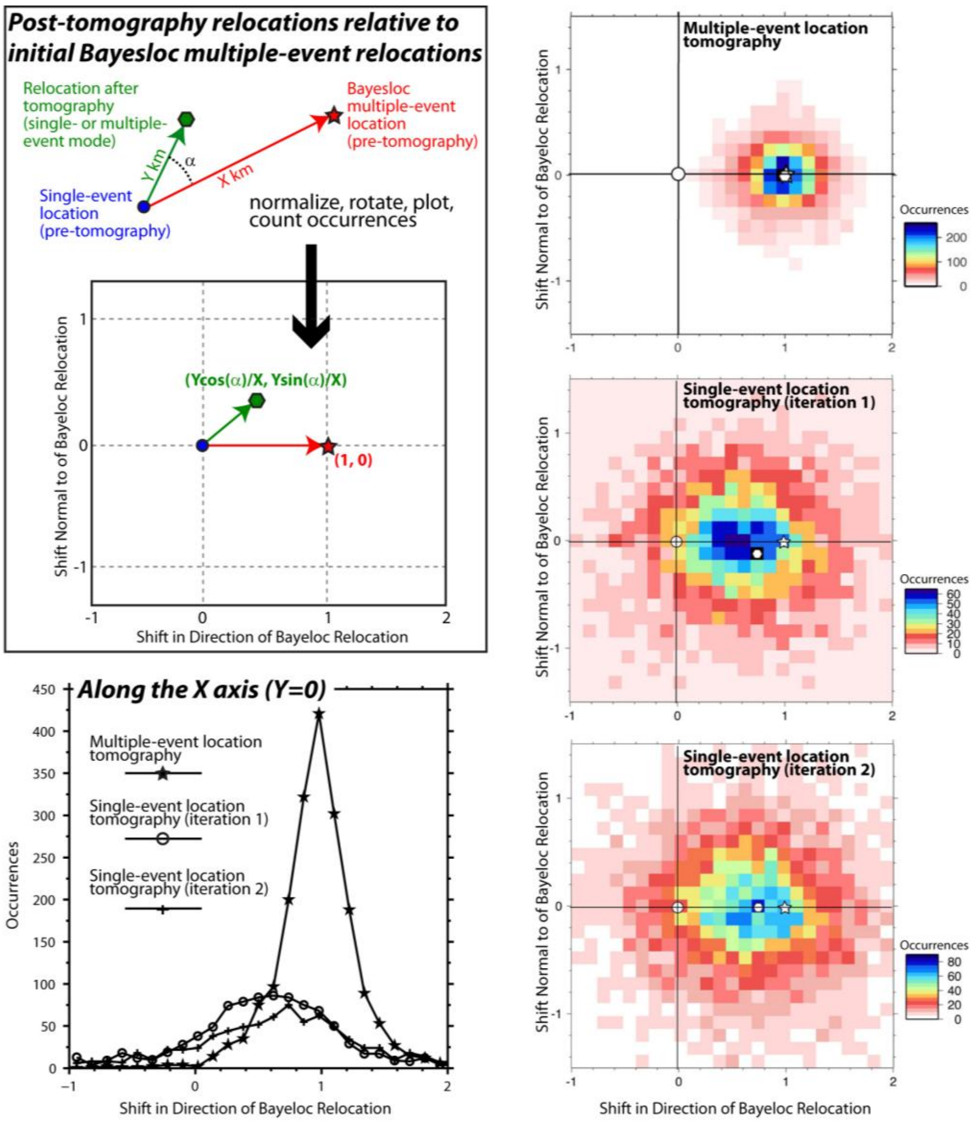

Figure 18 – relative relocation comparisons

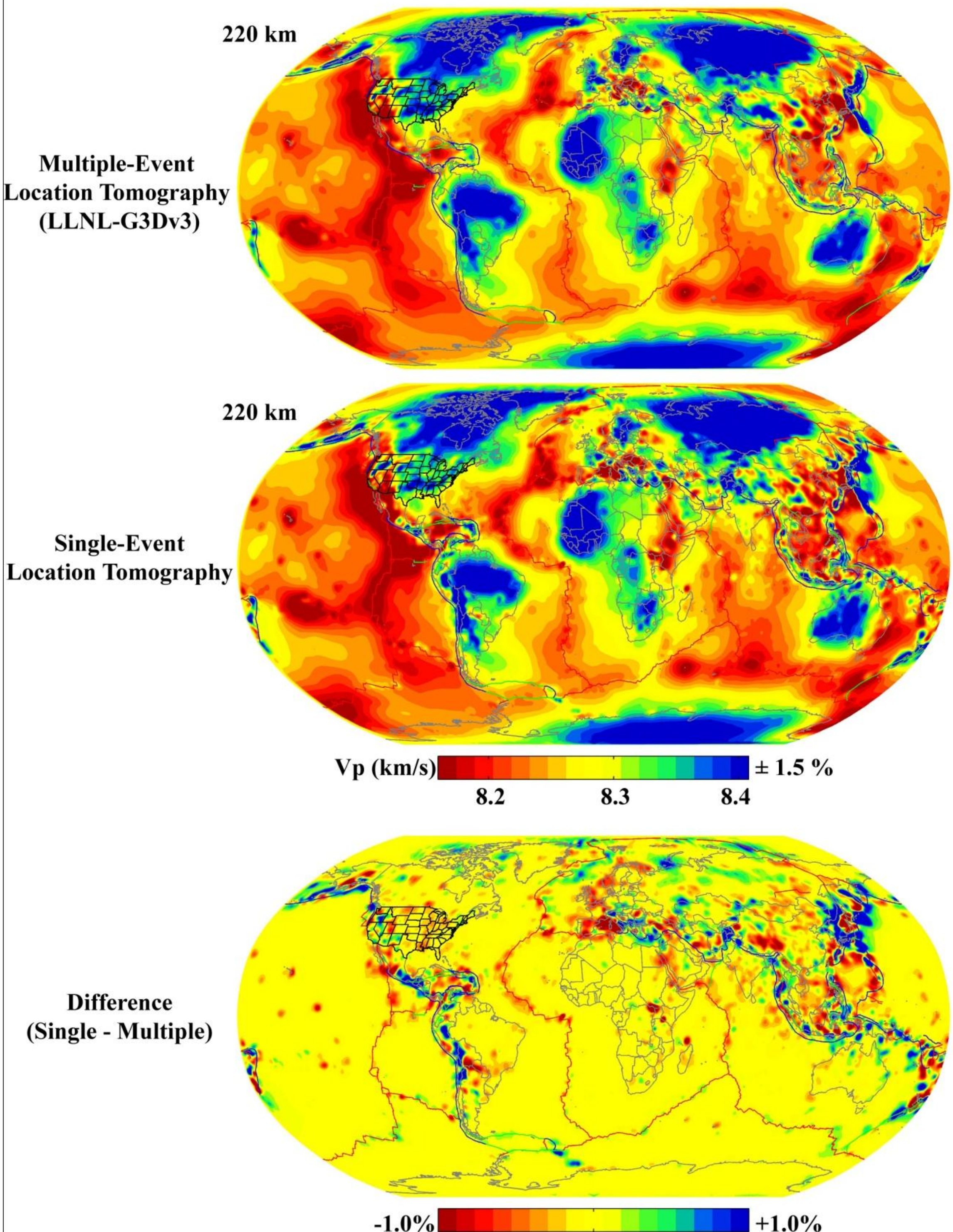

Figure 19 – Single-Multiple Event Location Model Comparison @ 220 km

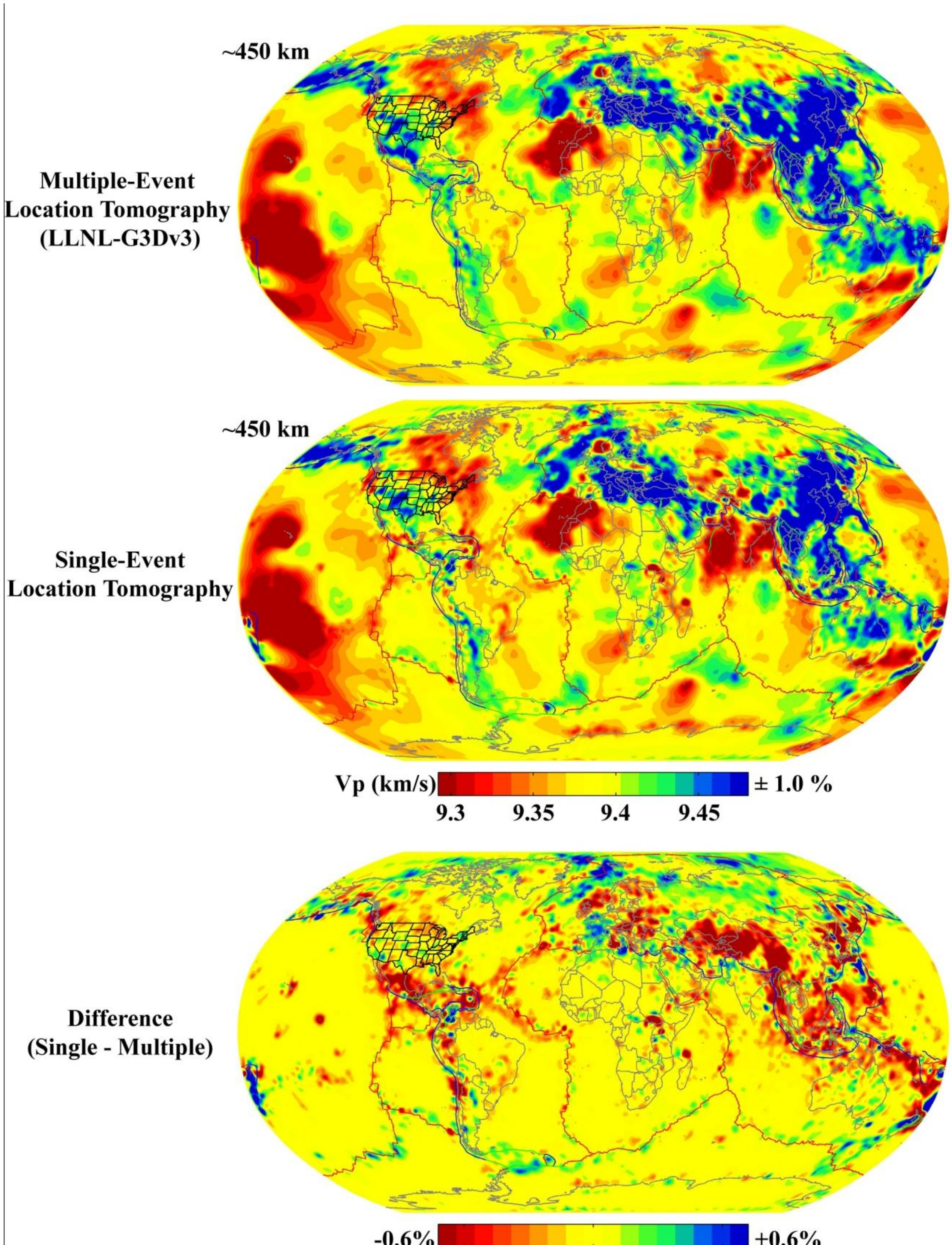

Figure 20 – Single-Multiple Event Location Model Comparison @ 450 km

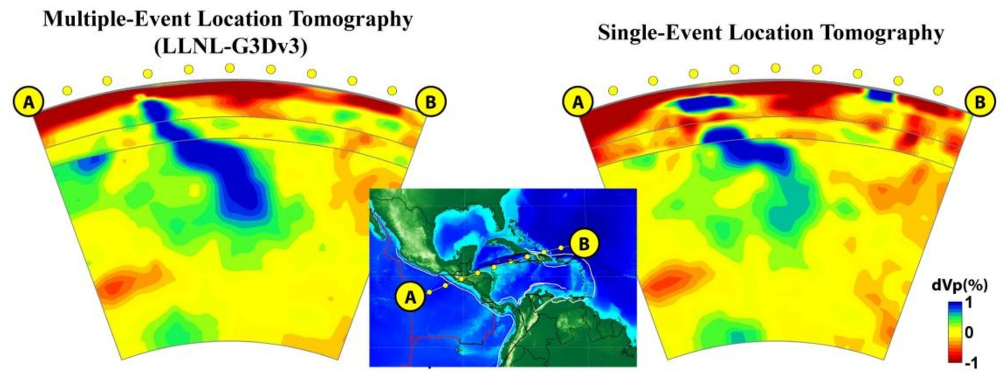

Figure 21 – Single-Multiple event location model comparison cross-section

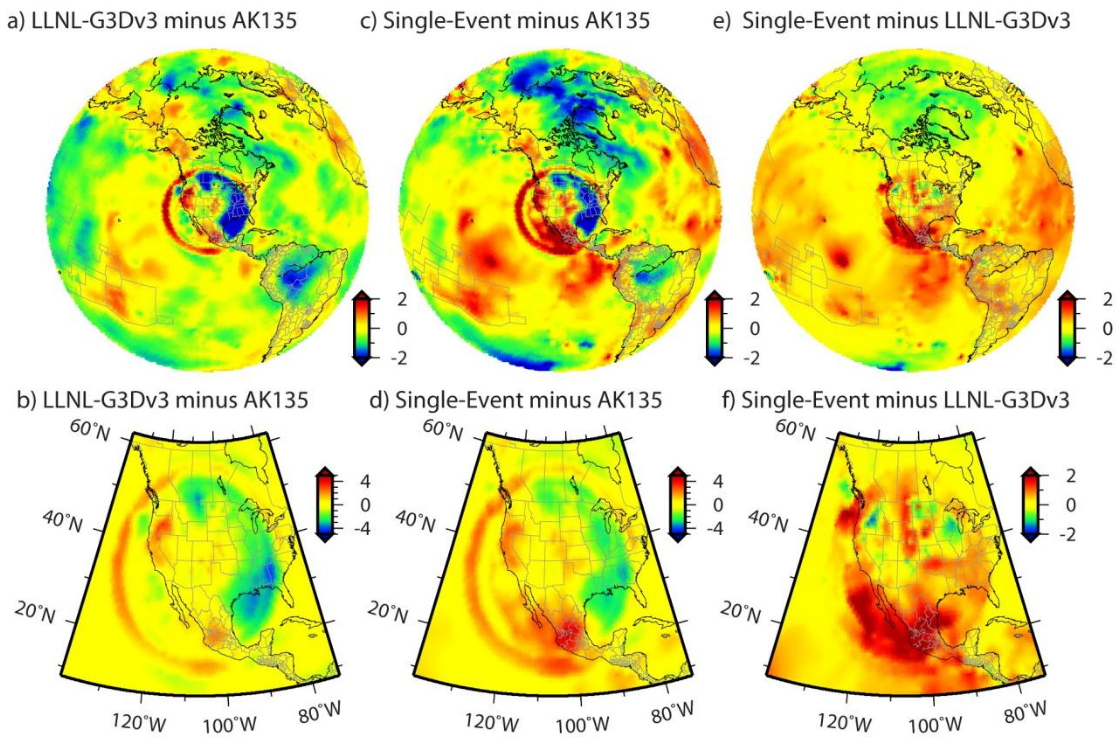

Figure 22 – Single-Multiple Event Model TT comparison (ANMO)

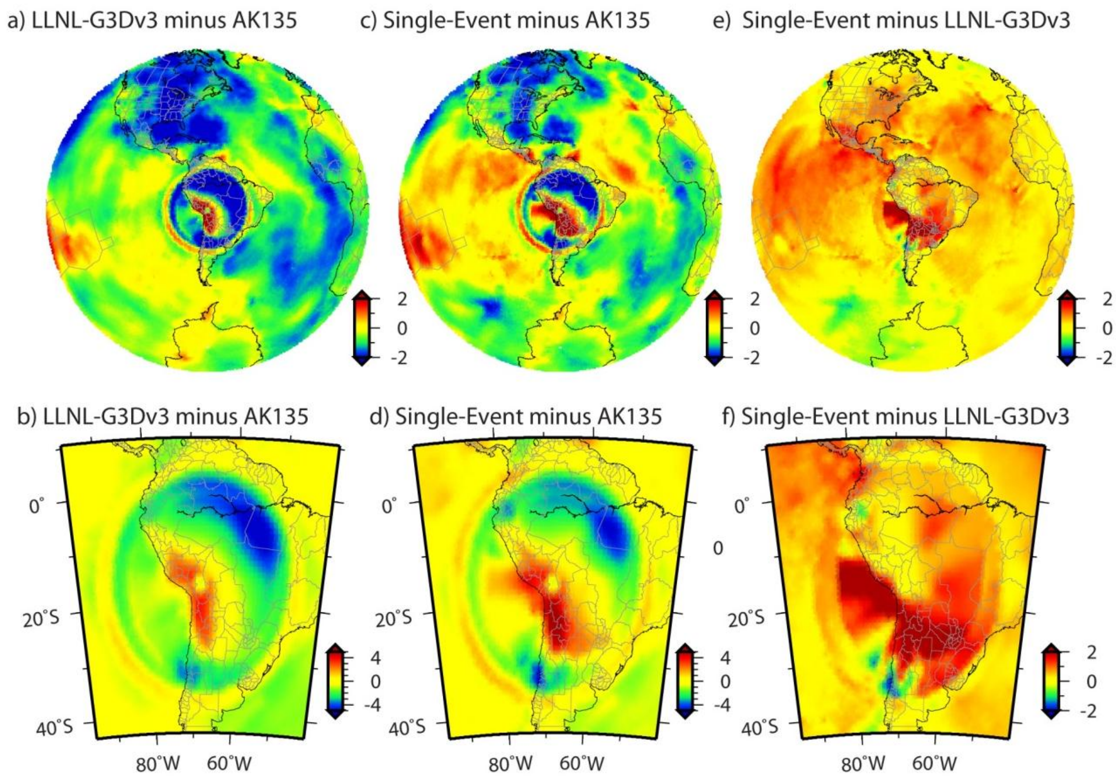

Figure 23 – Single-Multiple Event Model TT comparison (LPAZ)

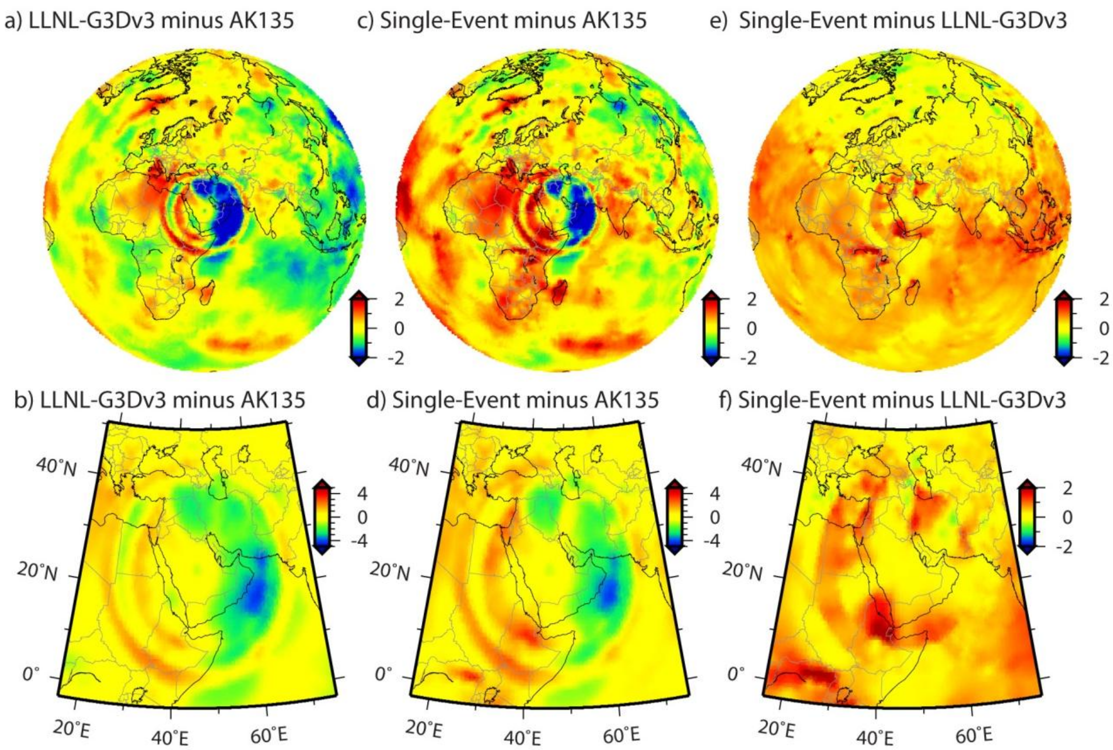

Figure 24 – Single-Multiple Event Model TT comparison (RAYN)

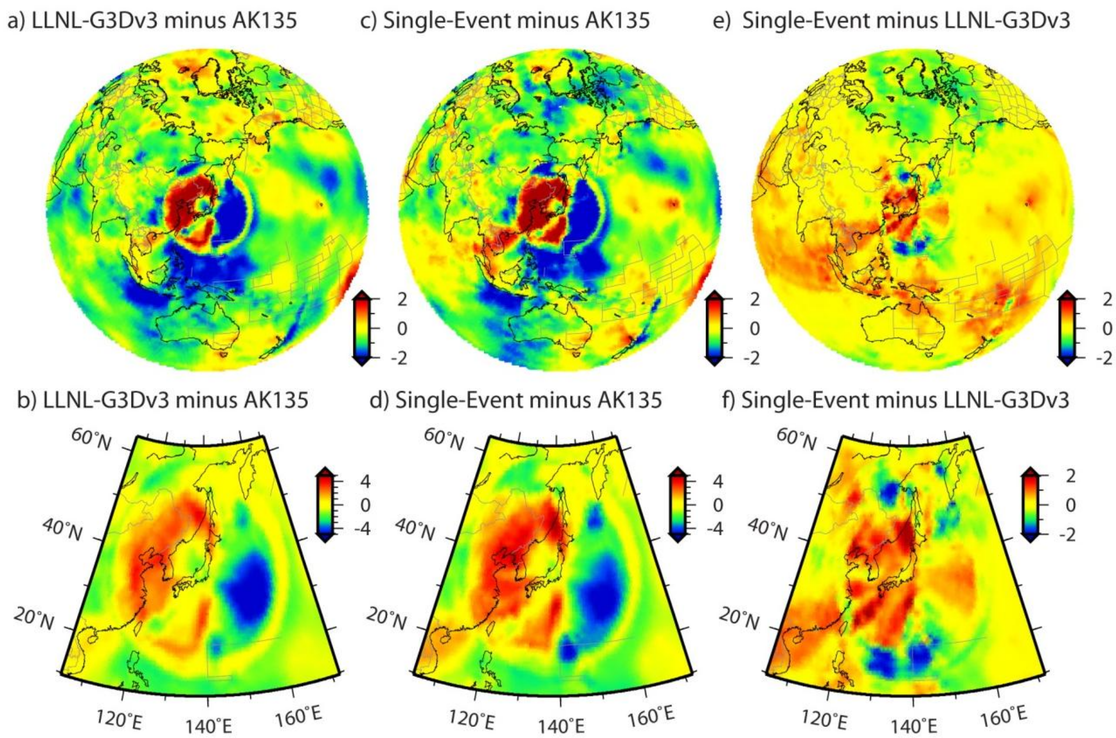

Figure 25 – Single-Multiple Event Model TT comparison (MAJO)